THESIS FOR THE DEGREE OF DOCTOR OF PHYLOSOPHY

IN

THERMO AND FLUID DYNAMICS

Numerical Simulations of Flows around Trains and Buses in Cross Winds

HASSAN NASR HEMIDA

Division of Fluid Dynamics

Department of Applied Mechanics

CHALMERS UNIVERSITY OF TECHNOLOGY

Göteborg, Sweden, 2008

Numerical Simulations of Flows around Trains and Buses in Cross Winds

HASSAN NASR HEMIDA

ISBN 978-91-7385-187-9

Doktorsavhandlingar vid Chalmers tekniska högskola
Ny serie nr: 2868
ISSN 0346-718X

Division of Fluid Dynamics
Department of Applied Mechanics
Chalmers University of Technology
SE-412 96 Göteborg, Sweden

Phone +46-(0)31-7721400
Fax: +46-(0)31-180976

This document was typeset using LaTeX
Printed at Chalmers Reproservice, Göteborg, Sweden 2008

Numerical Simulations of Flows around Trains and Buses in Cross Winds

by

Hassan Nasr Hemida

Division of Fluid Dynamics, Department of Applied Mechanics
Chalmers University of Technology, SE-412 96 Göteborg, Sweden

Abstract

When cruising in strong winds, ground vehicles can experience strong aerodynamic forces and moments that may increase drag, reduce their stability, generate noise and induce accidents in the case of strong side winds. However, prevention of the unwanted influences of side winds requires that the flow structures around vehicles are fully understood in both the instantaneous and time-averaged flow. The main objective of the present work is to acquire an understanding of the side wind flow physics around two types of ground vehicles, trains and buses.

In this work, Large-Eddy Simulation (LES) is used to compute the side wind flow around stationary simplified train models. The side wind flow is obtained at three different yaw angles, 30^o, 35^o and 90^o. The LES results show that the flow around high speed trains involves many small structures because of the instabilities of the shear layers that contribute to the time varying values of their aerodynamic forces and moments. The influence of the shape of the train nose on the flow field under side wind conditions is investigated. The LES results show that the shape of the nose determines to a large extent the characteristics of the wake structures and their associated frequencies. During the second part of the work, Detached-Eddy Simulation (DES) is used to investigate the flow structures around a double deck bus subjected to a 30^o yaw angle. The influence of gusty winds on the aerodynamics of buses is investigated by making simulations using different proposed wind gust profiles. The influence of the shape of the front of a double-deck bus on its aerodynamics is investigated in CFD simulations using the realizable $k-\epsilon$ RANS model at different designs of the front. The bus is subjected to a 30^o side wind. For the purpose of shape optimization, the response surface method was used and the optimum shape thereby obtained.

The influence of a passive flow control on the boundary layer and heat transfer is investigated by attaching small vortex generators on the surface of a heated, mounted cube. A more turbulent boundary layer is obtained behind the vortex generators and hence an enhancement in the heat transfer coefficient is observed.

List of Publications

This thesis is based on the work contained in the following papers:

Paper I H. Hemida, S. Krajnović and L. Davidson.
"Large-Eddy Simulations of the Flow around a Simplified High-Speed Train under the Influence of a Cross-Wind"
AIAA paper number AIAA-2005-5354, 2005.

Paper II H. Hemida and S. Krajnović.
"LES Study of the Influence of a Train Nose Shape on the Flow Structures under Cross-Wind Conditions". *Journal of Fluid Engineering*, 130, 9, 091101, 2008.

Paper III H. Hemida and S. Krajnović.
"Exploring the Flow around a Generic High-Speed Train under the Influence of Side Winds using LES"
Proc. CWE2006, Yokohama, Japan, July 2006.
Accepted for publication in Journal of Wind Engineering and Industrial Aerodynamics, 2008.

Paper IV H. Hemida and S. Krajnović.
"Exploring Flow Structures around a Simplified ICE2 Train Subjected to a 30^o Side Wind Using Large-Eddy Simulation" *(Article in press) Journal of Engineering Applications of Computational Fluid Mechanics, 2008.*

Paper V H. Hemida and S. Krajnović.
"DES of the Flow around a Realistic Bus Model Subjected to a Side Wind with a 30^o Yaw Angle"
The fifth IASME / WSEAS International Conference on FLUID MECHANICS and AERODYNAMICS, Athens, Greece, August, 2007.
(The paper has been awarded the best student paper in the conference)

Paper VI H. Hemida and S. Krajnović.
"Transient Simulation of the Aerodynamic Response of a Double-Deck Bus in Gusty Winds"
(Article in press) Journal of Fluid Engineering (2008).

Paper VII S. Krajnović and H. Hemida.
"On the Aerodynamics of High-Speed Trains using Computer Simulations"
15th International Symposium, Towards more Competitive European Rail System, Ziline, Slovakia, May, 2007.

Paper VIII H. Hemida and S. Krajnović. "Aerodynamic Shape Optimization of a Double-Deck Bus Subjected to a 30^o Side Wind using CFD and Response Surface Models",
Internal report 2008:04, Division of Fluid Dynamics, Chalmers University, 2008.

Paper IX H. Hemida, F. Spehr and S. Krajnović. "Local Heat Transfer Enhancement around a Matrix of Wall-Mounted Cubes using Passive Flow Control: A Large-Eddy Simulation".
Int. J. Heat and Fluid Flow, 29, 1258-1267, 2008.

Division of work between authors

The respondent produced all the results and wrote the manuscripts with the exceptions explicitly mentioned in this section. The objectives of the research presented, and the contents of each paper, have been discussed in detail with the corresponding co-author(s), who provided valuable comments and read and revised the manuscript.

In the work described in Paper I, the experimental photographs were digitally extracted from a scan of figures in a paper written by Chiu and Squire (1992) referred to in Paper I.

My contribution to Paper VII was to provide the CAD geometry and the results of the simulations for side wind around the ICE2 train and to read and revise the manuscript.

The second co-author in Paper IX (Franziska Spehr) carried out the the simulations on the cube with the second vortex generator and contributed to the writing of the manuscript.

The numerical simulations described in the first four papers were carried out using in-house code, written and developed by Professor

Lars Davidson and Dr. Håkan Nilsson, Chalmers University of Technology.

Other relevant publications

- S. Krajnović, H. Hemida and B. Basara
"Optimization of Aerodynamic Performance of Vehicles using Response Surface Models"
Robust Design Through Engineering Simulation, October 2008, Pôle Léonard de Vinci, Paris - La Défense

- S. Krajnović, H. Hemida and J. Georgii
"DES of the Flow Around a High Speed Train under the Influence of Wind Gusts"
7th International ERCOFTAC Symposium on Engineering Turbulence Modeling and Measurements, ETMM7, 4-6 June 2008, Amathus, Cyprus

- H. Hemida and S. Krajnović.
"LES Study of the Influence of the Vortex Generators on Cooling of Surface-Mounted Cubes"
Thermal Issues in Emerging Technologies, ThETA 1, Cairo, Egypt, Jan 3-6th 2007.

- S. Krajnović. and H. Hemida
"Aerodynamic Optimization of Vehicles using Computational Fluid Dynamics and Response Surface Methodology"
I Proceedings of the *XXI International Automotive Conference SCIENCE and MOTOR VEHICLES*, Beograd, 23-24 April 2007,ISBN/ISSN:978-86-80941-31-8

- H. Hemida and S. Krajnović.
"Parallel CFD Computations of Cross-Wind Stability on an ICE2 Train"
In Proceedings of the *PARA'06, WORKSHOP ON STATE-OF-THE-ART IN SCIENTIFIC AND PARALLEL COMPUTING*, Umeå, SWEDEN, 2006.

- H. Hemida and S. Krajnović
"Numerical Study of the Unsteady Flow Structures around a Train-Shaped Body Subjected to Side Winds"
In Proceedings of the *ECCOMAS CFD 2006*, September 5-8, Egmond aan Zee, The Netherlands, 2006.

- H. Hemida and S. Krajnović
"LES Study of the Impact of the Wake Structures on the Aerodynamics of a Simplified ICE2 Train Subjected to a Side Wind"
In Proceedings of the *Fourth International Conference on Computational Fluid Dynamics ICCFD4*, Ghent, Belgium, 10-14 July, 2006.

- S. Krajnović, H. Hemida and B. Diedrichs
"Time-Dependent Simulations for the Directional Stability of High Speed Trains Under the Influence of Cross Winds or Cruising Inside Tunnels"
In Proceedings of the *FLUID DYNAMICS APPLICATIONS IN GROUND TRANSPORTATION: "Simulation, a Primary Development Tool in the Automotive Industry"*, Lyon, France, 2005.

- Hassan Hemida and S. Krajnović
"Detached-Eddy Simulation of the Separated Flow over a Model Bus Subjected to Different Scenarios of Wind Gusts."
Internal Report, Division of Fluid Dynamics, Dept. of Applied Mechanics, Chalmers University of Technology, Göteborg, SWEDEN, reference number:2007-09.

- Hassan Hemida
"Large-Eddy Simulation of the Flow around Simplified High-Speed Trains under Side Wind Conditions"
Thesis of Lic. of Engineering, Division of Fluid Dynamics, Dept. of Applied Mechanics, Chalmers University of Technology, Göteborg, SWEDEN, ISSN 1652-8565, 2006.

Acknowledgments

This work would not have been possible without the support of a number of organizations and individuals. The research was carried out at the Division of Fluid Dynamics, Department of Applied Mechanics, Chalmers University of Technology, and was supported by the Swedish Agency for Innovation System (VINNOVA), Bombardier Transportation, and Scania.

I would like to acknowledge the Swedish National Infrastructure for Computing (SNIC), the High Performance Computing Center North (HPC2N), the National Supercomputer Center in Sweden (NSC) and the Center for Scientific Computing at Chalmers (C3SE). Ansys FLUENT Sweden AB is also gratefully acknowledged for providing the software licenses.

I would like to express my sincere gratitude to my supervisor, Associate Prof. Siniša Krajnović and my examiner, Professor Lars Davidson, for sharing some of their profound knowledge in computational fluid dynamics with me. This thesis would never have reached this point without their enlightening discussions and brilliant advice.

The interesting and stimulating discussions that arose at the steering group meetings are gratefully acknowledged, and my thanks go to Per Johnsson and Stephen Conway from Scania and Dr. Ben Diedrichs from Bombardier Transportation.

My warmest and deepest gratitude goes to my family, Fainan, Mayar and Momen, for their love and support.

Nomenclature

Upper-case Roman

A_{ij}	second order tensor
C_d	drag force coefficient
C_l	lift force coefficient
C_p	local pressure coefficient
C_s	side force coefficient and Smagorinsky model coefficient
C_Y	yaw moment coefficient
D	train height
F_d	drag force
F_l	lift force
F_s	side force
J_{ij}	Jacobian tensor
L	train length
M_p	pitching moment
M_r	rolling moment
M_y	yawing moment
P	first invariant of the velocity gradient
Q	second invariant of the velocity gradient
R	third invariant of the velocity gradient
Re	Reynolds number
S_{ij}	strain rate tensor
St	Strouhal number
U	velocity

Lower-case Roman

$a_i,\ b_i$	vectors in space
c_i	constant
f	frequency
p	pressure
t	time
t^*	dimensionless time unit

u_i	Cartesian components of the velocity vector
$x,\ y,\ z$	Cartesian coordinate vector components

Upper-case Greek

D	Total (material) derivative
Δ	filter width and matrix discriminant
Δt	time step
Ω_{ij}	rotation tensor

Lower-case Greek

δ_{ij}	Kronecker delta
θ	angle in a train cross-section
λ	tensor eigenvalues
μ	viscosity
ν	kinematic viscosity ($\nu = \mu/\rho$)
ν_t	turbulent kinematic viscosity
ρ	density
σ_{ij}	viscous stress tensor
τ_{ij}	subgrid scale stress tensor

Subscripts

t	turbulent quantity
o	initial condition
∞	free stream or ambient conditions

Superscripts

SGS	subgrid scale
$-$	spatially filtered quantity

Abbreviations

CFD	Computational Fluid Dynamics
CFL	Courant-Friedrichs-Levy
DNS	Direct Numerical Simulation
LES	Large Eddy Simulation
DES	Detached Eddy Simulation
RANS	Reynolds Averaged Navier-Stokes
S-A	Spalart-Allmaras

Contents

Chapter 1

Background

1.1 Introduction

As long as the sun shines, wind will blow carrying power that can be destructive for ground vehicles. Ground vehicles always suffer from wind in the forms of increasing drag, reduction in stability, noise generation and side wind induced accidents. Cruising in side winds results in the generation of aerodynamic forces and moments that tend to push the vehicle from the side and can turn it over. Obviously, the resulting forces and moments depend strongly on the speed of the vehicles; consequently, the threat of side winds becomes more serious as the speed increases.

The side wind influence on ground vehicles has long been investigated by the automotive industry. Often, a reduction in side wind sensitivity had to take second place to other driving situations. Recent developments in automotive engineering have been shown a trend toward faster, more energy efficient and more comfortable vehicles with a higher passenger capacity. These effects lead directly to light weight cars. Unfortunately, these developments have a significant negative effect on the side wind stability. As a result, optimization of the aerodynamic performance of ground vehicles has become one of the main objectives of the design process. Among the different issues of aerodynamics currently considered, side wind effects play an important role owing to their non-trivial impact on the rollover stability of vehicles.

1.2 Side Winds on Trains

When a high speed train cruises in a side wind, the effective side wind is strong even if the magnitude of the side-wind velocity is low. The effective side wind is the result of the speed of the train and of the side

wind. The angle between the effective side wind direction and the train cruising direction is the yaw angle, as shown in Fig. 1.1. The value of this angle is determined by the train cruising speed, the side wind speed and the side wind direction. Normally, side wind yaw angles are below 40^o owing to the relatively low speed side winds compared to the speed of the train. However, it is possible to find high speed trains that cruise at larger yaw angles, e.g. when they exit from tunnels or when a strong side wind has a strong component in the same direction as that of the train.

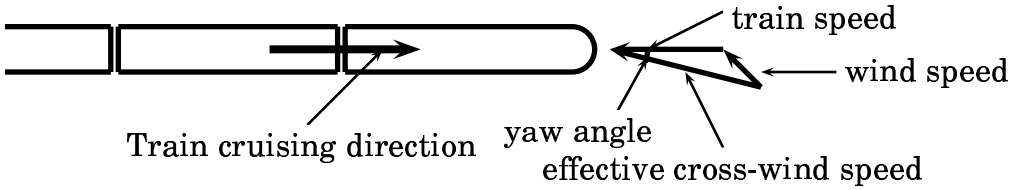

Figure 1.1: Effective side wind

The new generation of high speed trains is light in weight in order to provide high acceleration and to reduce the energy necessary to overcome gravity and friction forces. When these trains cruise in a strong side wind, there is a stagnation region with high pressure on the streamwise face while a region of low pressure is formed on the lee side due to the recirculation regions in the wake flow. In addition, the flow moves over the train roof at high velocity, making a region of low pressure on the upper side. Because of these pressure differences, high speed trains experience strong aerodynamic forces and moments such as side and lift forces and a yaw moment, as shown in Fig. 1.2. In such conditions, high speed trains are at high risk of overturning or derailing.

Although the railway accidents caused by side winds are rare compared to other ground vehicles, there have been 28 wind induced train accidents in Japan alone since Japanese railways started transport service in 1872 [Fujii *et al.* (1999)]. In Japan in 1986, seven coaches hauled by a heavy diesel locomotive were blown off Amarube Bridge to the ground by a strong wind, killing six people and wounding six others [Fujii *et al.* (1999)]. Diedrichs (2005) reported several railway accidents that occurred from 1880 to 2004. The most recent accident caused by known by the author was in the USA in 2004, where 68 empty grain cars from the Burlington Northern-Santa Fe train were derailed when it was returning from El Paso, Texas. The three locomotives pulling

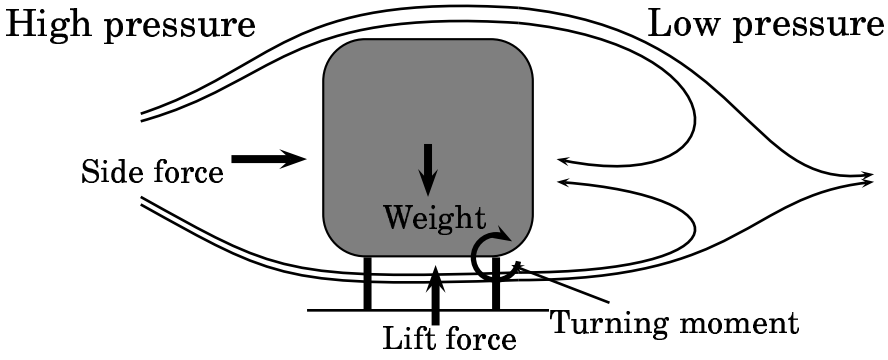

Figure 1.2: Aerodynamic forces and moments due to side wind.

the cars remained on the track. Figure 1.3 dives photographs of three further examples of railway vehicles that overturned due to side wind instability.

Figure 1.3: Examples of railway overturns due to cross wind instability. Left: France, Villy, 28.01.1994; middle: Japan, Sanriku Railway, 22.02.1994; right: Austria 17.11.2002. Taken from [Wu (2004)].

Previous experimental studies have concentrated mainly on the vehicle's response to the side wind and not very much on understanding the flow mechanisms. Prevention of the unwanted influences of a side wind requires that flow structures on the train surface and around it are fully understood in both the instantaneous and the time-averaged flow. Unsteady flow past a train in a side wind has been the object of numerous experimental investigations [Baker (2003); Baker *et al.* (2004); Chiu (1995); Chiu & Squire (1992); Copley (1987); Suzuki *et al.* (2003); Hoppmann *et al.* (2002)]. The primary interest in these investigations was measurements of some integral parameters such as drag, lift and side force coefficients together with measurements of the natural wind characteristics around the train. Some other researchers have investigated the flow structures numerically [Diedrichs (2003); Khier *et al.* (2000)] to obtain a better understanding of the flow behavior.

Most of these studies are based on Reynolds-averaged Navier-Stokes (RANS) equations or time varying RANS (URANS). Since the side wind instability is a consequence of the unsteadiness of the flow field around the train, an accurate time-dependent solution is necessary. Diedrichs (2005) made a comprehensive literature review of computational methods for cross-wind stability of railway trains. His study showed that most side wind investigations are based on the time-averaged solution. Here, only the mean flow is explored and the instantaneous information is lost.

1.3 Side Winds on Buses

Side wind problems in road vehicles are not better than those in trains. Furthermore, the most notable side wind induced accidents involve high-sided vehicles like buses and trucks with trailers. In theory, less tire friction means that lower wind speed is needed to cause the vehicle to slip. During windy conditions, a greater number of accidents occur when the road friction is lower than usual, due to water or ice. A wet road surface seems to be equally hazardous as an icy or snowy road surface. A possible explanation is that drivers seldom experience the reduced friction caused by a wet road surface and are thus not prepared for the combined effects of wind gust and reduced road friction, while, in contrast, an icy road triggers an "automatic reflex" in most drivers.

The natural side wind has a transient behavior, meaning that it varies in both time and space. This variation is due to the turbulence behavior of the natural wind. In some extreme cases the wind changes its speed rapidly to form a gust. In this particular case, the natural side wind may influence both the stability of the bus and the ride comfort of the passengers. In other cases, when a bus, for example, travels in a tunnel and no overtaking takes place, the influence of side winds is small. Once the bus leaves the tunnel it might encounter a strong wind from the side to form a gust in space that might also be variable in time. The influence of gusts is of a great concern in bus aerodynamics. The expected sudden change of forces and moments acting on a bus is believed to be a cause of several bus accidents. In November 1998, between Enköping and Sala in Sweden, a bus turned over and six people were killed. The Swedish accident investigation board concluded that the probable cause of the crash was the large lateral wind force that, in combination with a slippery road surface, made the coach impossible to steer the front wheels as they lost the necessary road grip [SHK (2001)]. In October 1995, a bus with 41 passengers went off the

road in a high side wind and rolled over. The accident occurred when the bus was driving north alongside a narrow fjord in the northwest of Iceland. This resulted in two passengers being killed and leaving the others with minor to severe injuries [Ragnar & Jonas (1998)].

Many researchers have investigated the influence of steady side wind on vehicles [Chiu & Squire (1992); Suzuki *et al.* (2003); Baker *et al.* (2004); Baker (2003); Hemida & Krajnović (2008); Krajnović *et al.* (2008); Esra & Bedii (2004); Hucho & Sovran (1993); Baker & Reynolds (1992); Kobayashi & Kitoh (1983)]. On the other hand, few investigations have been made to study the influence of gusty wind on vehicles. It is difficult, however, to investigate the aerodynamics of a real vehicle in gusty wind. Instead, numbers of wind tunnel investigations have been carried out in the last four decades to quantitatively measure the aerodynamics of vehicles in gust. Some EU projects have been initiated in recent years to study the influence of gusts on vehicles [Diedrichs (2005); Matschke (2001); DEUFRAKU Project (2004)]. Ryan & Dominy (2000) experimentally investigated the wake behind a passenger car subjected to a cross wind gust. The aerodynamics of the MAGLEV train in gust were also experimentally investigated by HOWELL (1986). He found that the aerodynamic coefficients for the MAGLEV train are similar to those of a planar track except for the side force coefficient. Because of the difficulties of modeling the natural gust, few numerical simulations are found in the literature. Clarke & Filippone (2007) numerically studied the aerodynamics of two vehicles in overtaking. Their study was limited to two-dimensional models. Some other reports in the literature dealt with analytical investigations of the gust response [Filippone (2003); Patrick & Christophe (2004); Baker (1991)]. Cheli *et al.* (2006) used a generic model for the aerodynamic forces caused by a gust to analytically study the dynamic response of a heavy vehicle. The side wind on buses has recently been given great attention since several vehicle accidents have been traced to side wind, especially when it is accompanied with a gust [Juhlin (2005); Petzäll *et al.* (2008); Hemida & Krajnović (2007)]. The flow structures around buses and their aerodynamic response during the gust, however, are not properly investigated in the literature. A suitable wind gust model for numerical investigation that takes into account the dynamic behavior of a typical gust is also lacking to the knowledge of the author.

1.4 Shape Optimization

It is known that the aerodynamics of vehicles depends on their shape. Thus a vehicle's side wind resistance can be improved by adjusting its design. The geometrical shapes of vehicles are complex, and many variables can be optimized to enhance their aerodynamics. Moreover, the flow around vehicles is very complex, which makes it difficult to develop accurate and reliable design tools to predict an optimal shape. The design of the vehicles has traditionally been based on simplified analytical methods and model tests. Optimization has been handled in a trial-and-error design procedure that relies on the skills and experience of the aerodynamicist.

Thanks to the recent improvements of numerical methods in Computational Fluid Dynamics (CFD) and the development of high performance computing capabilities, complex and realistic problems for industrial applications are now addressed by engineers using numerical simulations. Aerodynamic shape optimization is one of the engineering fields that has greatly benefited by this development. Because of the large number of experiments that might be needed to find the optimum vehicle shape, a CFD based design can further be aided by a robust and user friendly optimization framework. In the present work, the focus was on finding an optimal shape of a double-deck bus subjected to side wind using CFD and a surrogate based algorithm.

The outcome of a CFD based bus shape design or model test may not necessarily lead to the best possible shape. In addition, optimization of the aerodynamic properties of a vehicle is always a multi-objective (drag, lift, side force, aerodynamic moments) problem (MOP). Moreover, several aerodynamic objectives are known to be in conflict. For instance, reducing the drag of a bus by changing its shape often produces a high lift or a high side force. A resulting optimum shape should then be a compromise between these objective functions. There is thus a great need of a more systematic approach, capable of identifying and comparing different trade-offs of multi-objective design. Numerical prediction of the flow around a bus subjected to side wind is however challenging and time consuming. Hence, there is a great need of reliable and accurate CFD models, together with efficient and effective optimization frameworks. The increase in computer power has recently made possible the use of CFD in the design process in the automotive industry. Some research papers address the use of CFD in the optimization of the nose of a simplified train in order to improve the aerodynamic performance of a train subjected to side wind [Krajnović (2007*a*,*b*)]. Others have addressed the use of CFD to find the optimum shape of a vortex generator to reduce the drag of a train [Krajnović &

Hemida (2007); Krajnović (2007*b*,*c*,*a*)].

1.5 Heat transfer and vortex generators

The electronic component is a bluff body, which produces flow with separations. The flow around an integrated electronic circuit can be approximated to be similar to the flow around a cube mounted on a surface. When electronic components are attached to a printed circuit, they, under concentrated heat dissipation conditions, act as a strong source of heat that might cause local overheating. It is generally believed that local overheating of integrated circuits (IC) is the major cause of the technical failure of electronic equipment. Hence, finding a way to efficiently remove heat for from these components is crucial to ensuring steady, reliable, long-term operations. The production and development of a new generation of power electronic components is controlled by the efficient design to remove the heat that they generated. In general, heat removal from an integrated circuit depends greatly on the flow structures around it.

Previous investigations of the flow around a surface-mounted cube found that different kinds of flow instabilities give rise to different flow structures around the cube. The flow separates from the side of the cube to form separation bubbles. The flow inside these bubbles circulates and it might be trapped in place if the bubbles are steady. The shear layers between these separation bubbles and the exterior fluid are highly turbulent, and this gives rise to so-called Kelvin-Helmholtz flow instability. This flow instability is responsible for the shedding of vortex tubes in a regular fashion to the wake flow behind the cube, distortion of large scale vortices, production of small scales and eventually transition from laminar to turbulent flow. There is also flow instability in the wake flow behind the cube, which is associated with the shedding of large scale vortices from the recirculation region to the far wake flow.

This flow instability is controlled by the flow Reynolds number and hence the high frequency mode in the shear layers between the recirculation region and the exterior fluid. The dominant shear layers around the cube make the flow structures very complicated.

Different numerical methods have been used in the past to study the flow around a single cube mounted on a surface. Krajnović & Davidson (2000) and Krajnović & Davidson (2002) used large-eddy simulation to investigate the flow structures around a surface-mounted cube in a fully developed channel flow. They used different techniques to visualize the flow. In their simulation, the Reynolds number was 40000 based on the incoming mean bulk velocity and the height of the cube.

They found that the flow separates from the surface of the cube on the lateral and the top side faces of the cube. They visualized a horse-shoe vortex attached to the surface on which the cube is mounted, as shown in Fig. 1.4.

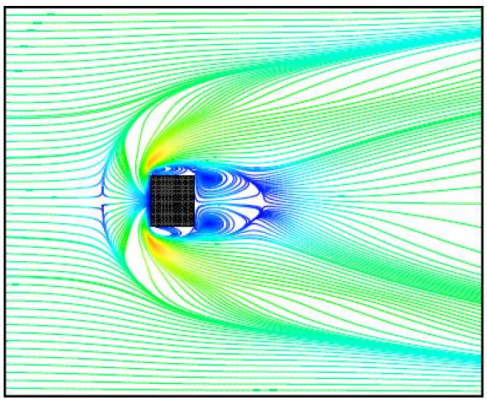

Figure 1.4: Streamlines of the mean flow projected onto the channel floor, [Krajnović & Davidson (2000)]

Cone-like vortices are formed on the top side face. These complex flow structures are obtained using different flow simulations. The results are in good agreement with the experimental results of Martinuzzi & Tropea (1993), who made measurements in a low speed wind tunnel. Yakhot *et al.* (2006) studied the same cube at the relative low Reynolds number of 1870, based on the incoming bulk velocity and the height of the cube, using Direct Numerical Simulation (DNS) and they observed similar flow structures.

The local heat transfer around a wall-mounted cube has also been studied. Nakamura *et al.* (2003) experimentally discovered the heat transfer of a cube oriented 45 ° to flow direction to be lower than that of a cube oriented perpendicular to the flow at the range of Reynolds numbers $4.2 \times 10^3 - 3.3 \times 10^4$.

The turbulent flow around multiple cubes is even more complicated. The wake structures from one cube interact with the structures of the other cubes and the surface on which they are mounted. The flow is characterized by the complex interior topology, which induces the flow to separate and recirculate locally between the mounting surface and the cubes. The shedding of the large scale structures in the wake flow depends mainly on the Reynolds number of the flow and on the separation distance between the cubes. The flow structures, however, are highly unsteady and three dimensional.

An enhancement of heat transfer can be achieved by altering the turbulent boundary layer on the surfaces of the cubes. This is done by generating small vortices on the surface of the cube using different vortex generators (VG).

A VG can be any kind of small scale device used to cause local mixing by generating a trailing vortex. Appropriate VG installations result in a transfer of higher momentum fluid towards the inner part of the boundary layer. Re-energizing the inner boundary layer in this way will delay or even prevent boundary layer separation. VGs are widely used to delay the flow separation to control the boundary layer and to decrease the drag coefficient of vehicles [Koike *et al.* (2004)]. Figure 1.5 (a) shows VGs attached to the rear window of a road vehicle for drag reduction. VGs are very often attached to the aircraft wing, as shown in Fig. 1.5(b), to increase the lift coefficient. VGs are also used in gas turbines to reduce flow separation, and hence the pressure drop. Another application of vortex generators is to enhance the heat

(a) VG attached to the back side of a car [Mitsubishi (2006)].

(b) VG attached to a wing of an airplane [Online (2006)].

Figure 1.5: Examples for vortex generators

transfer of a cooling surface. Here, it is highly desirable to have turbulent boundary layers that imply high mixing of the fluid particles. This can be arranged by the small scale vortices produced by the vortex generators, and in fact leads to a better convective heat transfer than without vortex generators. For this purpose the vortex generators should be tiny bluff bodies attached to the cooling surface at the position at which separation of the flow would start without them.

In the case of multiple cubes behind each other, vortex generators can also change the size of the recirculation region in the wake of one

cube and thereby change the incoming flow to the next cube.

1.6 Objectives and delimitation

The main objectives of this thesis are to acquire an understanding of the physics of the flow around trains and buses subjected to cross winds and its influences on the aerodynamic coefficients using an accurate transient CFD method. The flow around a surface mounted cube is similar to that of the flow around a vehicle, since it is dominated by flow separations and reattachments. Hence, a small part of this work is devoted to studying the influence of attaching vortex generators to the surface of a cube, mounted in the middle of a matrix of surface mounted cubes, on heat transfer.

The work of this thesis is divided into five parts with different objectives, summarized in the following items.

- *Flow around trains subjected to side winds.* Two simplified models are used to investigate the influence of the side winds on trains: one is a generic, where its profile follows a simple mathematical equation, and the other a simplified ICE2 train. The influence of the movement of the ground is not included here. The models are subjected to side winds at different yaw angles and Reynolds numbers. Despite the simple geometry of the models, the flow shows a high degree of complexity for small and large yaw angles, where different kinds of flow instabilities are found.
- *Influence of the nose shape of a train on flow structures and its aerodynamics when subjected to side winds.* Here, the focus is on the influence of the shape of the train nose on the flow structures and aerodynamics. Two different models are used in the investigations, which are identical in dimensions and shape while one nose length is double that of the other.
- *Flow around a double-deck bus subjected to side winds.* Although buses are bluff bodies, the flow structures around them are expected to be different than those around trains. A transient numerical method is used here to investigate the flow structures around a double-deck bus subjected to a 30^o yaw angle. The available experimental data for the aerodynamic coefficients of such a bus shows that the 30^o yaw angle is the most critical yaw angle the bus can encounter. The influence of a wind gust on the aerodynamics of buses is investigated by making different simulations at the same yaw angle using different proposed wind gust profiles.

- *Shape optimization of a bus subjected to side winds.* The objective here is to show the CFD combined with the surface response method to be a cheap tool for shape optimizations. The design variables are the front curvature and front angle of a double-deck bus while the objective functions are the aerodynamic coefficients.

- *Use of vortex generators to enhance the heat transfer around a matrix of surface-mounted cubes.* Traditionally, vortex generators (VGs) are used for drag reduction in the aeronautical and automotive industries. They are also used to reduce separation in gas turbine ducts. Here, we aim to use the VGs to enhance heat transfer by mounting them on the surface of a heated cube subjected to forced convection. The objective is to investigate its influence on the momentum and thermal boundary layers.

It is worth mentioning here that the objective of this thesis is not to find a way to avoid the unwanted influence of the side winds. Instead the work presented here offers a full picture of the flow field around simplified trains and buses subjected to crosswinds, at relatively low Reynolds numbers. This will hopefully help engineers to better understand the flow around similar bodies at higher Reynolds numbers and prevent the unwanted influences of side winds.

1.7 Outline of the thesis

This thesis is based on nine appended papers, of which four have been accepted for publication in well known scientific journals (two have been published and two are in press). The first two appended papers deal with the flow around a generic train at a 90^o yaw angle. In particular, the influence of the nose shape on the flow structures is included in the second paper. The influence of the yaw angles on the flow structures and aerodynamics of trains is demonstrated in Papers 3 and 4. Papers 5 and 6 present flows around buses subjected to different scenarios of wind gust. The response surface method used for shape optimization is demonstrated in Papers 7 and 8. Finally, the use of VGs for cooling surface-mounted cubes is reported in Paper 9. All research results are included in the papers, which are summarized in Chapter 5. To make the scope of the thesis comprehensible for a wider audience, the following three chapters are dedicated to non-experts of fluid dynamics. Most of the visualization methods used in this work is briefly explained in Appendix A.

Chapter 2

Flow Around Trains and Buses

The flow around trains and buses is different from that past airplanes and other air and space vehicles because the interaction between the underside flow and the ground cannot be ignored. Owing to the geometrical characteristics and operational speeds of trains and buses, the resulting flow field is essentially a three-dimensional turbulent one. Generally, the associated variations in density are negligible, and the flow may be treated as incompressible. However, for specific cases (tunnel entry, extremely high speeds), compressibility effects have to be taken into consideration.

The ultimate goal of any aerodynamic design process is to enhance the aerodynamic characteristics of an initial geometry with respect to certain functional requirements. Executing such optimization under operational and sometimes stylistic constraints requires an extensive understanding of the underlying flow physics. Moreover, the relationship between the resulting forces and moments and the flow structure has to be explained.

2.1 Aerodynamic coefficients

When trains or buses cruise in a side wind they experience aerodynamic forces and moments. The aerodynamic forces are the drag force, F_d, which resists the forward motion of the vehicle, the lift force, F_l, which acts upward and tends to raise the vehicle up from the ground, and the side force, F_s, which pushes the vehicle from the side. The latter is a result of the side wind. The aerodynamic moments that arise due to side wind are the rolling moment, M_r, the pitching moment, M_p, and the yawing moment, M_y. Figure 2.1 shows the different aerody-

namic forces and moments on a train subjected to a side wind. The magnitude of these forces and moments depends on the Reynolds number and the shape of the train.

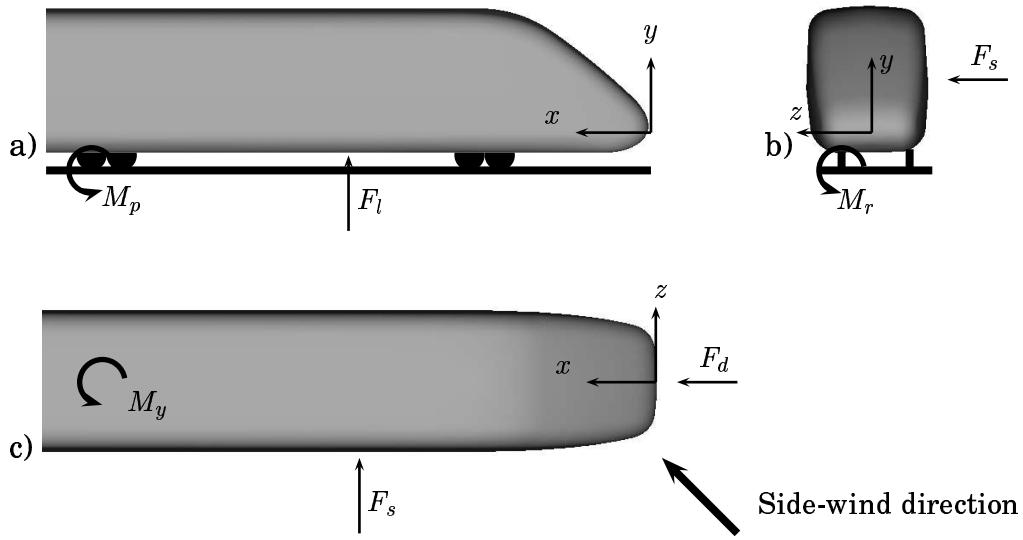

Figure 2.1: Forces and moments acting on trains under the influence of a side wind. a) View from a side b) Front view c) View from above.

It is useful to have a simple means to compare the aerodynamic forces produced by different vehicle shapes, regardless of their size or driving speed. This is conveniently provided by factors called aerodynamic coefficients, which depend mainly on the shape of the vehicle and the direction of the side wind. The drag coefficient, C_d, the lift coefficient, C_l, and the side force coefficient, C_s, are defined as:

$$C_d = \frac{\int p_s dA_x}{\frac{1}{2}\rho {U_\infty}^2 A_x}, \tag{2.1}$$

$$C_l = \frac{\int p_s dA_y}{\frac{1}{2}\rho {U_\infty}^2 A_y} \tag{2.2}$$

and

$$C_s = \frac{\int p_s dA_z}{\frac{1}{2}\rho {U_\infty}^2 A_z} \tag{2.3}$$

where p_s is the surface pressure, and A_x, A_y and A_z are the projected surface areas in the x, y and z directions, respectively.

In certain flow regimes, the effect of Reynolds number on the aerodynamic coefficients can be quite pronounced. The coefficients can change dramatically over the Reynolds number region, which encompasses a transition from laminar to turbulent boundary layers. However, in other flow regimes, the effect of the Reynolds number is much weaker. As a result, aerodynamic coefficients are often considered to be rather weak functions of Reynolds number and a strong function of yaw angle.

It is convenient to express the pressure distribution in terms of the pressure coefficient, C_p, which is defined as:

$$C_p = \frac{p - p_\infty}{\frac{1}{2}\rho {U_\infty}^2} \tag{2.4}$$

where p is the local static pressure, U_∞ is the free stream velocity and p_∞ is the free stream static pressure. The difference between the local static pressure, p, and the free-stream static pressure, p_∞, depends directly on the dynamic pressure of the free stream, $1/2\rho {U_\infty}^2$. Therefore, the pressure coefficient remains constant at all speeds.

2.2 Flow Structures Around Trains

From the fluid mechanics point of view, trains can be categorized as moving bluff bodies of a high slenderness ratio. The structures of the flow around trains depend on the flow Reynolds number and yaw angles. Copley (1987) investigated the influence of Reynolds number on the flow field around a train when it is subjected to a cross wind. He found that, for very low Reynolds number, the flow around the train is laminar everywhere and remains attached to the train surface. Increasing the Reynolds number results in a separation on the roof side close to the streamwise edge and the detachment of the flow from the face, as shown in Fig. 2.2.a. At the same time, the wake begins to shed vortices in a regular fashion. A further increase in Reynolds number makes the flow fully turbulent in the wake and in the separation region over the roof-side face. At some critical Reynolds number, the flow reattaches to the face, forming a separation bubble, as shown in Fig. 2.2.b. For higher Reynolds number, this separation bubble is suppressed and the flow over the roof-side face is fully attached, as shown in Fig. 2.2.c. However, although the influence of the shape of a train nose is believed to play an important role in the flow structures and aerodynamics of high speed trains and influences the value of the Reynolds number at which the flow becomes fully attached, it has not yet been properly investigated.

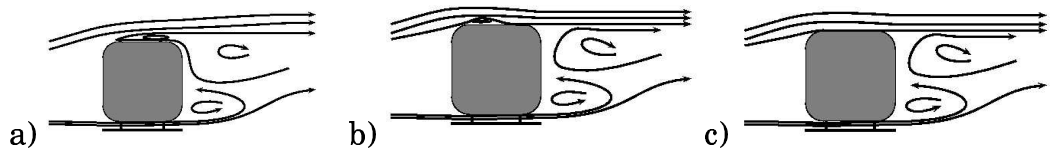

Figure 2.2: Effect of Reynolds number on the flow structures around train under cross wind conditions.

Numerical and experimental studies of the flow around bluff bodies [Krajnović & Davidson (2004); Singh & Mittal (2005); Kravchenko & Moin (2000); Mittal & Moin (1997); Constantinuescu & Squires (2003)] show that such flows are highly unsteady and three dimensional. Moreover, when the Reynolds number is high enough to obtain a fully turbulent flow in the shear layers and in the wake, two main instability modes are present in the wake. The first is the large-scale shedding in the wake, and it manifests itself as a progressive wave motion with alternate fluctuations produced by the shear present at the limit between the recirculation zone and the exterior fluid. These fluctuations determine the periodic shedding of the vortices that form behind the bluff body. The second high frequency mode is so called spiral mode, which is associated with the small scale, shear layer Kelvin-Helmholtz instability on the periphery of the recirculation region where shear flow is present, as shown in Fig. 2.3. This instability is responsible for the distortion of the large vortex structures, shedding of the vortex tubes in a quasi-coherent fashion inside the detached shear layers, production of the small scales, and, eventually, transition to turbulence in the wake (for more detail see Constantinuescu & Squires (2003)).

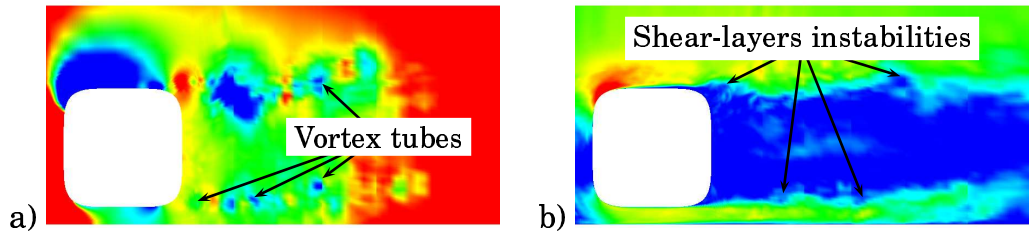

Figure 2.3: Cross section of the LES flow around trains in a cross wind showing the shear layer instabilities colored by (a) the instantaneous static pressure and (b) the magnitude of the instantaneous velocity vector.

Capturing these structures and investigating the flow features require simulation methods that resolve, rather than model, the main dynamics governing the flow. Numerical solutions using URANS are not able to capture these high frequency modes since the Reynolds stresses representing the turbulence in URANS are modeled with a turbulence model. Finding a true representation of the flow is dependent on the turbulence model used. Moreover, it is difficult to define a model that can accurately represent the Reynolds stresses in the region of separated flow, such as the wake behind a train. The discretization schemes play important roles in determining these structures. Since the high frequency modes in the train boundary layers and shear layers are important in side-wind simulations, the convective flux, the viscous diffusion and the sub-grid fluxes should be approximated by a second order accurate central difference scheme to reduce the numerical dissipation that arises from using upwind schemes. This dissipation suppresses the formation of the small eddies and hence the formation of high frequency modes.

2.3 Flow Structures Around Buses

The flow around a bus is similar to the flow around a cube, which is dominated by flow separation and reattachment. Since the cross section shape of buses is similar to that of trains, the influence of the Reynolds number on the flow around buses is similar to its influence on the flow around trains.

(a) 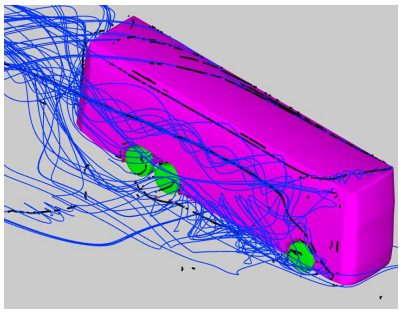 (b) 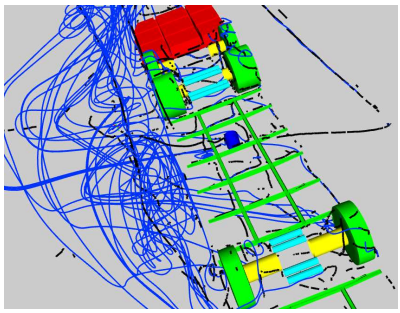

Figure 2.4: Streamlines generated from the vortex cores of flow around a bus subjected to a side wind: (a) flow structures around the bus, (b) flow structures around the chassis of the bus.

Krajnović (2002) conducted extensive numerical studies of the flow around a simplified bus. The bus was not subjected to any side wind.

He found that the flow is very complex. It separates on the rounded leading edges of the bus and forms two lateral vortices (one on each side of the body) and one vortex on the roof of the bus. The flow separates on the rear edges of the body and forms four vortices: one on the top, one on the bottom and one on each side, each with its axes parallel to its separation edge. The flow around buses subjected to side winds is more complex. The side flow terminates the symmetrical behavior of the flow and new vortical structures are born in the lee-side flow. The boundary layer thickness is also different since the distance the flow moves over the bus surface is shorter. Figure 2.4 shows the flow structures around a bus subjected to a side wind by means of streamlines generated from the vortex cores.

Chapter 3

CFD and Turbulence Modeling

Since analytical methods cannot be employed except in a limited number of simple cases, the aerodynamic design of ground vehicles relied mainly on experimental techniques. During the past three decades, computational fluid dynamics (CFD) has evolved as a new discipline in fluid mechanics. Complementing the two classical branches of fluid mechanics, CFD has enabled large steps to be made in various fields of research, especially aerodynamics. Despite its success in numerous areas, the large computational demands required for those applications related to ground vehicles has made its use rather limited. However, the advent of modern, high performance computers brought CFD to the scene of vehicle aerodynamics.

The application of CFD becomes attractive when experimental investigations are expensive, not applicable or are difficult to perform. In general, experimental techniques demand intensive time and financial resources. Total alleviation of these drawbacks through the use of scale wind tunnels is not possible because of Reynolds number restrictions. For a non-trivial number of flow cases, reproduction of some specific boundary and/or operating conditions in wind tunnels is beyond realization. On the other hand, open air testing is governed primarily by atmospheric conditions, which makes the replication of experiments extremely difficult.

3.1 Turbulent Flow

Turbulence is the natural state of many flows. It differs from laminar flow in the way that its attributes, such as velocity or pressure, fluctuate in both time and space. There is no precise and unique definition

of turbulence, but one can see turbulent flow as a tangle of vortices. The turbulent motions are often generated in the flow as a result of the three-dimensional flow instabilities. These instabilities are concentrated near the solid boundaries and behind bluff bodies. This is why the turbulent flow starts first in the boundary layer and then spreads to the external flow. It can be seen by studying transitional flow over a flat plate, for instance. In the case of bluff bodies, the flow instabilities and hence the transition to turbulence depend on the size of the body, l, the velocity of the fluid, u, and the kind of fluid, which is described for example by the kinematic viscosity, ν. These properties can be combined to obtain the Reynolds number, Re:

$$Re = \frac{u\,l}{\nu}. \tag{3.1}$$

By increasing the Reynolds number, the flow behind the body becomes more and more likely a turbulent flow. Figure 3.1 shows the flow structures around a circular cylinder at different Reynolds numbers. At very low Reynolds numbers, the flow is laminar everywhere and the flow instability, due to the existence of the cylinder, is too small to generate turbulent flow (see Fig. 3.1 (a)). When the Reynolds number is increased further, an adverse pressure gradient arises at the surface of the cylinder. Because of this adverse pressure gradient, the flow is likely to separate from the surface of the cylinder. Separation occurs if the inertia of the flow, the convective part in the Navier-Stokes (Eq.3.9), is not high enough to overtake the adverse pressure gradient. Owing to the flow separation, the flow instability is strong enough to initiate turbulence in the wake (see Fig. 3.1 (b)). At that point, the flow is turbulent only in the wake of the cylinder and is laminar upstream and in the boundary layers. At high Reynolds numbers, the flow separates from the surface of the cylinder and is completely turbulent in the wake and in the boundary layer (see Fig. 3.1 (c)).

The critical value of Re for the flow to develop a fully turbulent wake is about 10^5.

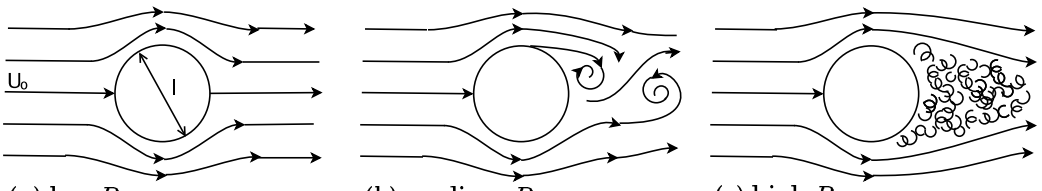

(a) low Re (b) medium Re (c) high Re

Figure 3.1: Flow around a cylinder at different Reynolds numbers Re

The point at which the flow separates from the surface is called the

separation point. The position of this point on the surface of the cylinder depends mainly on the Reynolds number. Depending on the shape of the bluff body, the flow may form a separation bubble and reattach to the surface. The separation bubble is the region that enclosed the flow between the separation point and the reattachment point. The separation bubble is always associated with low pressure inside the bubble. Moreover, the temperature of the flow in the separation bubble is higher than the surrounding flow temperature if the separation occurs next to a heated surface. This is because some of the high temperature fluid might be trapped and be circulating inside the separation bubble.

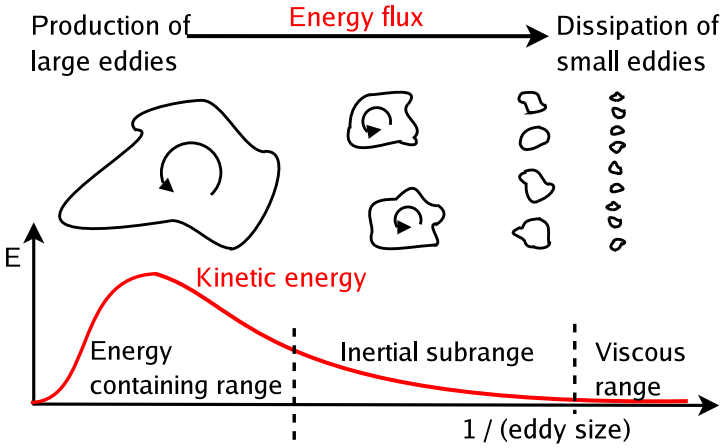

Figure 3.2: Energy cascade of a turbulent flow

In the case of high Reynolds number flow, there exists a broad spectrum of length scales. The largest vortices in the flow are characterized by the size of the body that created them. This is called the integral length scale, l. The large scale eddies take their energy from the mean flow. They are unstable and break up into smaller scale eddies, which themselves are also unstable, and they pass their energy to even smaller scale eddies. This is called the energy cascade and is shown schematically in Fig. 3.2. The wide field of length scales, η, in the turbulent flow ranges from the integral length scale, l, to the smallest length scale of the flow. Besides the length scale, η, there are two other scales of the motion, the time scale, τ, the time needed for an eddy to turn over, and the velocity scale, v, which is $v = \eta/\tau$.

The viscosity plays no important part in the energy cascade, as long as $Re = \frac{v\eta}{\nu} >> 1$. The viscous forces can be neglected compared to the inertial forces at those high Reynolds numbers, but when the vortex becomes small enough, the viscous forces are significant and the eddy

disappears at the end. The energy of the vortex never disappears but is converted to internal energy of the flow by raising its temperature.

The size of the smallest scales of the motion was described by Kolmogorov (1941). These smallest scales depend only upon the dissipation of kinetic energy, ϵ, and the kinematic viscosity, ν. The Kolmogorov microscales are:

$$\eta_K \equiv (\nu^3/\epsilon)^{1/4}, \;\; \tau_K \equiv (\nu/\epsilon)^{1/2}, \;\; v_K \equiv (\nu\epsilon)^{1/4}. \tag{3.2}$$

Close to the solid boundaries, the scales of the flow are very small and are of the same order of magnitude as the Kolmogorov microscales. The Reynolds number based on the turbulent scales in that region is very small and the dissipation of kinetic energy is very high.

3.1.1 Incompressible Flow

If the density, ρ, of all fluid particles is constant, the flow is called incompressible flow. This does not imply that the density is the same everywhere in the fluid. The density may vary in space and time, but it must do so in precise way.

$$\frac{D\rho}{Dt} = \frac{\partial \rho}{\partial t} + u_j \frac{\partial \rho}{\partial x_j} = 0\,, \tag{3.3}$$

where t, u_j and x_j are the time, velocity of the flow and coordinates, respectively. No fluid is truly incompressible, but one may say a flow is almost incompressible if the density variations of the fluid particles are negligibly small compared to the variation of flow velocity.

$$\frac{\partial \rho}{\partial x} << \frac{\partial u}{\partial x}\,. \tag{3.4}$$

To decide whether to treat a flow as incompressible or not, the dimensionless Mach number, M, is useful. This compares the fluid velocity with the speed of sound,

$$M = \frac{\text{fluid velocity}}{\text{speed of sound}} = \frac{u}{a}\,. \tag{3.5}$$

For ideal gas,

$$a = \kappa\,\frac{p}{\rho} = \sqrt{\kappa R\,T}$$

and equation 3.5 can be written as:

$$M = \frac{u}{\sqrt{\kappa R\,T}}\,, \tag{3.6}$$

where κ is the ratio of specific heat, R is the gas constant and T is the temperature.
For $M < 0.2$, the flow is incompressible and sub-sonic. Thus one can say that the flow of liquids or gases is incompressible if their velocity is small. The flow in ventilation ducts and the flow around ground vehicles (except perhaps for very high speed trains ≈ 400 km/h) can be considered to be incompressible and sub-sonic, for instance.

3.1.2 Governing Equations in Fluid Dynamics

The conservation laws can be applied to fluid dynamics to deduce equations governing the motion of the flow.
The continuity equation can be derived from the law of conservation of mass. Using the Cartesian tensor notation, the resulting equation is:

$$\frac{\partial \rho}{\partial t} + \frac{\partial(\rho u_i)}{\partial x_i} = 0, \quad i = 1, 2, 3 \ . \tag{3.7}$$

For incompressible and Newtonian flow, Eq. 3.7 can be written as:

$$\frac{\partial u_i}{\partial x_i} = 0 \ . \tag{3.8}$$

The principle of momentum conservation can be applied to the same fluid to deduce the momentum equations (Navier-Stokes equations). It can be written as a nonlinear partial differential equation:

$$\frac{\partial u_i}{\partial t} + u_j \frac{\partial u_i}{\partial x_j} = -\frac{1}{\rho}\frac{\partial p}{\partial x_i} + \nu \frac{\partial^2 u_i}{\partial x_j \partial x_j}, \tag{3.9}$$

where p is the instantaneous pressure. The kinematic viscosity, ν, and the dynamic viscosity, μ, are connected over ρ as follows:

$$\nu \equiv \mu/\rho \ . \tag{3.10}$$

The conservation of energy yields to the following equation for incompressible flow, neglecting heat transfer by radiation:

$$\frac{\partial T}{\partial t} + u_j \frac{\partial T}{\partial x_j} = \frac{\nu}{Pr}\frac{\partial T}{\partial x_j \partial x_j} + \frac{1}{c}\epsilon_{ij} \ , \tag{3.11}$$

where c is the specific heat capacity, which is a quantity of the fluid. The specific heat capacity, c, for air is about 1.005 $\frac{J}{kg\ K}$. The variable ϵ represents the dissipation of energy. It is defined as:

$$\epsilon_{ij} = 2\nu \, (\frac{\partial u_i}{\partial x_k}\frac{\partial u_j}{\partial x_k}). \tag{3.12}$$

The properties of turbulent flow seem to fluctuate randomly. A statistical approach can be used after decomposing the flow into a mean part and a fluctuating part as:

$$\begin{aligned} u &= \overline{u} + u^{'}, \\ p &= \overline{p} + p^{'}, \\ T &= \overline{T} + T^{'}. \end{aligned} \tag{3.13}$$

In many cases, it is easier to analyze time-averaged flow and to compare modified flow situations, while the instantaneous flow already differs for the same flow problem over time.

The time average of a flow variable such as $f(\vec{x},t)$ is defined by

$$\overline{f(\vec{x},t)} = \lim_{\Delta t \to \infty} \frac{1}{\Delta t} \int_{t}^{t+\Delta t} f(\vec{x},t)dt\,. \tag{3.14}$$

Using the decomposed variables of the flow, the continuity equations and the momentum equations can be written in a form similar to the Reynolds-averaged Navier-Stokes equations:

$$\frac{\partial \overline{u_i}}{\partial x_i} = 0, \;\; \frac{\partial u_i'}{\partial x_i} = 0 \tag{3.15}$$

and

$$\underbrace{\rho\frac{\partial \overline{u_i}}{\partial t}}_{\text{time dependence}} + \underbrace{\rho\overline{u_j}\frac{\partial \overline{u_i}}{\partial x_j}}_{\text{convection}} = \underbrace{-\frac{\partial \overline{p}}{\partial x_i}}_{\text{pressure term}} + \frac{\partial}{\partial x_j}\Big(\underbrace{\overbrace{\rho\nu}^{=\mu}\frac{\partial \overline{u_i}}{\partial x_j}}_{\text{viscous stress}} \underbrace{-\rho\overline{u_i'u_j'}}_{\text{Reynolds "stresses"}} \Big). \tag{3.16}$$

The last term in Eq. 3.16 represents the turbulent Reynolds stresses, $-\overline{u_i'u_j'}$. This term represents the influence of the turbulent motion on the averaged flow. There are no fluctuating scales in equation (3.16) since it is an equation for the averaged motion. However, that makes it useful in studying turbulence. Due to the fact that the Reynolds stresses are unknowns, there are fewer available equations than are demanded by the variables (the closure problem).

Neglecting the dissipation, the energy equation for time-averaged flow can be written as:

$$\begin{aligned} \frac{\partial \overline{T}}{\partial t} + \frac{\partial \overline{T}\,\overline{u_j}}{\partial x_j} &= \frac{\partial}{\partial x_j}\Big[\frac{\nu}{Pr}\frac{\partial \overline{T}}{\partial x_j} - (\overline{T}u_j' + T'\overline{u_j} + T'u_j')\Big] \\ &= \frac{\partial}{\partial x_j}\Big[\frac{\nu}{Pr}\frac{\partial \overline{T}}{\partial x_j} - (\overline{T\,u_j} - \overline{T}\,\overline{u_j})\Big]. \end{aligned} \tag{3.17}$$

Pr stands for the Prandtl number, which is a dimensionless quantity of the fluid. It describes the ratio between the viscous diffusion rate and the thermal diffusion rate.

Direct Numerical Simulation (DNS), Reynolds-Averaged Navier-Stokes Simulation (RANS), Large Eddy Simulation (LES) and Detached Eddy Simulation (DES) are methods to numerically solve for the pressure, p, velocity, u_i, and temperature, T, of the fluid in space and time.

3.2 Direct Numerical Simulation (DNS)

Making Direct Numerical Simulations (DNS) means numerically solving the governing equations of the flow to generate the exact instantaneous motions in a computer. These equations are the Navier-Stokes equations (3.9), the continuity equation (3.8) and the energy equation. The energy equation is not coupled with the continuity equation and the momentum equation in the case of incompressible flow. Hence, the continuity and momentum equations can be solved first and the temperature field can be obtained afterwards by solving the energy equation. In contrast, these equations are coupled and should be solved together in the case of compressible flow.

No assumptions or simplifications are needed for DNS, since the number of equations is equal to the number of unknowns (u_i, p and T). The minimum vortex size that can be obtained from the numerical simulation is the size of the cell, Δ. Thus, to resolve all the scales of the flow, the cell size should be of the same size as the smallest scales in the flow, the Kolmogorov dissipation scales,

$$\eta_K \sim l \cdot Re^{-3/4},$$

where l is the integral length scale and Re is the Reynolds number based on the integral scales.

The number of cells needed for DNS increases with the Reynolds number. The time step, Δt, required by DNS should be very small to resolve the flow in time. There are two factors that control the choice of the time step. It should be smaller than the Kolmogorov time scale, τ_K, and, in order to maintain numerical stability and accuracy, the time step should be small enough that the fluid particles do not move more than one grid spacing in each time step. This yields:

$$\Delta t = \min(\tau_K, \tfrac{\Delta x}{u}).$$

DNS is therefore restricted to low or moderate Reynolds numbers.

For high Reynolds numbers, the flow is dominated by very fine structures associated with very small scales. The total number of cells needed to resolve all the scales is very high and hence the computational cost is also very high. This makes DNS in feasible at the present time for solving high Reynolds number flow. At low Reynolds numbers, it is a useful tool in fundamental research of turbulence. Using DNS, one can perform "numerical experiments", and extract from them information difficult or impossible to get in the real laboratory, allowing a better understanding of the physics of turbulence.

However, even if our computers were able to solve a more complicated flow in an adequate time, we would sometimes need to average the huge random data in order to understand turbulence. It may sound easier to average the governing equations in the beginning and then to solve them afterwards. That could be done by simulating Reynolds-averaged Navier-Stokes equations (RANS).

3.3 Reynolds-Averaged Navier-Stokes (RANS)

There are six extra terms in the Reynolds-Averaged Navier-Stokes (RANS) equations (3.16). These terms are called Reynolds stresses. Hence, there are more unknowns than equations. This is a manifestation of the *closure problem* and the reason why we need turbulence models. There exist mainly two different kinds of turbulence models, the turbulent viscosity models and the Reynolds stress models. The turbulent viscosity models act on the assumption that the Reynolds "stresses" can be acquired analogously to the viscous stress term, because it also resists the flow motion in some way. This leads to:

$$-\overline{\rho u_i' u_j'} = \mu_t(\frac{\partial \overline{u}_i}{\partial x_j} + \frac{\partial \overline{u}_j}{\partial x_i}) - \frac{2}{3}\rho K \delta_{ij} \,. \tag{3.18}$$

Here, δ_{ij} is the Kronecker's delta, defined as:

$$\delta_{ij} = \begin{cases} 1 & \text{if } i = j \\ 0 & \text{otherwise} \end{cases},$$

and K is the kinetic energy, expressed as:

$$K = \frac{1}{2}\overline{u_i' u_i'}.$$

The second term on the right hand side of equation (3.18) is there to balance the equation when $i = j$.
The turbulent dynamic eddy viscosity, μ_t, has to be modeled, as it is

not a property of the fluid but a feature of the flow. It is not constant but depends on position and time. Some models describe this with algebraic equations and some use partial differential equations.
The Reynolds stress models characterize all the six terms separately by differential transport equations. The $k-\epsilon$ model, commonly used with RANS, is briefly described in Appendix B.

3.4 Large Eddy Simulation (LES)

Large eddy simulation (LES) decomposes the structures of the flow into large and small scales. The large motions of the flow are directly simulated while the influence of the small scale on the large scale motions is modeled. Hence LES is a kind of compromise between RANS and DNS.

LES consists of four conceptual steps:

(i) Filtering
In this step, the actual velocity, $u_i(\vec{x},t)$, is decomposed into a filtered part and a sub-grid component of velocity.

$$u_i(\vec{x},t) = \underbrace{\overline{U_i}(\vec{x},t)}_{\text{filtered component}} + \underbrace{U_i'(\vec{x},t)}_{\text{sub-gridscale component}}, \tag{3.19}$$

where $\overline{U}_i$ represents the motion of the large eddies and U_i' is the residual velocity field.

In the same way, the temperature, T, is filtered as well:

$$T(\vec{x},t) = \overline{T}(\vec{x},t) + T'(\vec{x},t).$$

(ii) Solving the filtered velocity field
The equations for the large scale eddies can be derived from the Navier-Stokes equations by inserting Eq. 3.19 and filtering it afterwards. It is analogous to the derivation of the Reynolds-averaged Navier-Stokes equation. As in general, the filtered sub-grid velocity does not equal zero and second filtering yields a different result from the first filtering:

$$\overline{U'}_i \neq 0 \text{ and } \overline{\overline{U}_i} \neq \overline{U}_i.$$

The filtered continuity and momentum equations for incompressible flow are:

$$\frac{\partial \overline{U}_i}{\partial x_i} = 0 \,, \tag{3.20}$$

and

$$\rho\frac{\partial \overline{U_i}}{\partial t} + \rho\frac{\partial \overline{U}_j\overline{U}_i}{\partial x_j} = -\frac{\partial \overline{p}}{\partial x_i} + \frac{\partial}{\partial x_j}\left(\mu\frac{\partial \overline{U_i}}{\partial x_j} - Q_{ij}\right), \tag{3.21}$$

where Q_{ij} are the residual stresses defined as:

$$Q_{ij} = \overline{U_i'U_j'} + \overline{U_i'\overline{U_j}} + \overline{\overline{U_i}U_j'} = \overline{u_iu_j} - \overline{U}_i\overline{U}_j \,.$$

Similarly, the filtered energy equation arises as:

$$\frac{\partial \overline{T}}{\partial t} + \frac{\partial}{\partial x_j}(\overline{U}_j\overline{T}) = \frac{\nu}{Pr}\frac{\partial^2\overline{T}}{\partial x_j\partial x_j} - \frac{\partial h_j}{\partial x_j}. \tag{3.22}$$

Here h_j represents the unknown sub-grid heat fluxes. They are defined as:

$$h_j = \overline{u_jT} - \overline{U}_j\overline{T} \,.$$

(iii) modeling the residual stress tensor and the sub-grid heat fluxes

The turbulence models for the residual stresses are analogous to the models used for the Reynolds stresses by RANS. The simplest one was proposed by Smagorinsky 1963. It models the SGS Reynold stress analogously to the way this is done in the eddy viscosity models.

$$Q_{ij} \simeq \overline{U_i'U_j'} = 2\nu_{SGS}\overline{S}_{ij} \,, \tag{3.23}$$

where S_{ij} is the resolved strain rate tensor, defined as:

$$\overline{S}_{ij} = \frac{1}{2}\left(\frac{\partial \overline{U}_i}{\partial x_j} + \frac{\partial \overline{U}_j}{\partial x_i}\right), \tag{3.24}$$

and ν_{SGS} is the sub-grid scale viscosity, which can be written as:

$$\nu_{SGS} = (C_S\,\Delta)^2\sqrt{2\overline{S}_{ij}\overline{S}_{ij}}. \tag{3.25}$$

Here, C_S is the model constant, which is often called Smagorinsky's coefficient and ranges from 0.06 to 0.2. The sub-grid scale, Δ, is the cubic root of the volume of the cell, $\Delta = (\Delta_1\Delta_2\Delta_3)^{1/3}$. It

should be of about the same magnitude as the filter width.
Using the Smagorinsky model, the sub-grid heat fluxes can be written as:

$$h_j = -\alpha_{SGS}\frac{\partial \overline{T}}{\partial x_j}\,. \tag{3.26}$$

Here, α_{SGS} is the sub-grid scale eddy diffusivity and, using Pr_{SGS} for the sub-grid Prandtl number, it is defined as:

$$\alpha_{SGS} = \frac{\nu_{SGS}}{Pr_{SGS}} = \frac{1}{Pr_{SGS}}(C_s\Delta)^2\sqrt{2\overline{S}_{ij}\overline{S}_{ij}}\,. \tag{3.27}$$

More information about sub-grid scale modeling can be found in Pope (2001); Wilcox (2002); Davidson (2004).

(iv) Numerically solve for the large eddy velocity
The last step is to solve the filtered Eqs. 3.21 and 3.22 to get the large eddy velocity field, $\overline{U}_i$, and the temperature, $\overline{T}$.

The computational cost of LES is low compared to that of DNS, since all the turbulent scales are not resolved. In LES, the large eddies are solved directly and the influences of the the small scale eddies on the large scale eddies are modeled. The size of the smallest scale eddy that can be resolved in LES is the size of the cell in the grid. Thus the grid spacing should be adequate, that is, slightly smaller than the size of the smallest energy containing motions.

Of course, the computational expense of LES is higher than that of RANS, but it is more accurate for flow in which large scale unsteadiness is significant, such as the flow around bluff bodies.

3.5 Detached Eddy Simulation (DES)

In the DES approach, the unsteady RANS models are employed in the near-wall regions, while the filtered versions of the same models are used in the regions away from the wall, i.e. LES. The LES region is normally associated with the core turbulent region where large turbulence scales play a dominant role. In this region, the DES models recover the respective sub-grid models. In the near-wall region, the respective RANS models are recovered. One of the commonly used turbulent models with DES, in the case of external flow, is the one-equation Spalart-Allmaras (S-A) model. The standard S-A model is explained briefly in Appendix C.

In the standard S-A model, the distance to the closest wall is used as the definition of the length scale, d, which plays a major role in determining the level of production and destruction of turbulent viscosity.

The DES model replaces d everywhere with a new length scale, $\tilde{d}$, defined as

$$\tilde{d} = \min(d, C_{\text{des}}\Delta) \tag{3.28}$$

where the grid spacing, Δ, is based on the largest grid space in the x, y, or z direction forming the computational cell. The empirical constant, C_{des}, has a value of 0.65.

Chapter 4

Response Surface Method

4.1 Introduction

Computational fluid dynamics (CFD) is able to simulate various kinds of flows for different applications and with a varying degree of approximation of the governing physics. The key idea behind shape optimization for fluids is to optimize a certain cost function on the basis of a simulation by changing specific geometry features, for example, to minimize the drag of a ground vehicle to save fuel but without changing the magnitude of the lift from that of the initial geometry. There are several different optimization techniques and approaches. The selection of the most suitable is highly problem dependent. One common design methods is the surrogate model approach, which aims at building models of the true objective and constraint functions. These models are able to numerically reproduce the physics of the problem at hand. In this work, a surrogate model approach, namely the response surface methodology (RSM), was adopted.

The response surface method has been widely used in practical engineering design optimization problems, where the optimal searches are based on the response surfaces mimicking the physical processes or models. The response surface method is sometimes the only practical option for performing design optimization, such as simulation based design optimization when the simulations are usually computationally expensive. In conventional approaches, the response surfaces are usually built up using a group of sampling points based on certain design of experiment (DOE) schemes. The accuracy of the response surface depends largely on the number of sampling points and their distributions in the design space, as well as the approximation functions for the response surface.

4.2 Response Surfaces

The response surface (RS) methodology is a statistical tool that is useful for modeling and analysis in situations in which the response of interest is affected by several input factors. The response surface method has been widely used in practical engineering design optimization problems, where the optimal searches are based on the response surfaces mimicking the physical processes or models. The RS method is sometimes the only practical option for performing design optimization, such as simulation based design optimization, when simulations are usually computationally expensive. In conventional approaches, the response surfaces are built up using the group of sampling points based on the DOE scheme. The approximation of the true response in an RS can be represented by low-order polynomials. For RS, polynomials are advantageous in that their coefficients can easily be determined using the least square method and, in that, a statistical evaluation can be made of them once their coefficients have been determined. For this reason, function approximations using the least square method are most often used with the response surface methodology.

A quadratic polynomial reads

$$\hat{y} = \beta_0 + \sum_{i=1}^{n} \beta_i x_i + \sum_{i=1}^{n} \beta_{ii} x_i^2 + \sum_{i=1}^{n} \beta_{ij} x_i x_j. \tag{4.1}$$

Representing the above with two variables for simplicity gives:

$$\hat{y} = \beta_0 + \beta_1 x_1 + \beta_2 x_2 + \beta_{12} x_1 x_2 + \beta_{11} x_1^2 + \beta_{22} x_2^2. \tag{4.2}$$

The CFD computed value can be expressed as:

$$y = \hat{y} + \epsilon, \tag{4.3}$$

where ϵ is the error between the computed and fitted values, as shown in Fig. 4.1. The regression coefficient, β, can be determined by minimizing the sum of squares of this error.

The goodness of the fit of RS with the data is measured using the coefficient of multiple determination, R^2, which takes the form:

$$R^2 = SS_R/SS_T = 1 - SS_E/SS_T. \tag{4.4}$$

Here, SS_E is the sum of the squared approximation errors at the n sampling points, SS_T is the true response's sum of squared variation

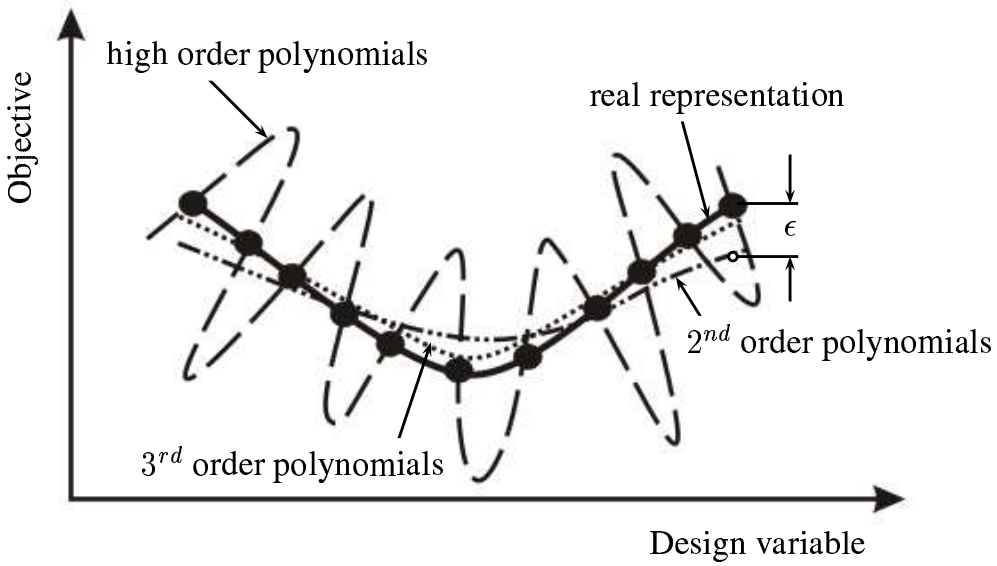

Figure 4.1: Approximation of the true response using polynomials.

from the mean, $\bar{y}$, and SS_R is the approximation's sum of squared variations from the mean, i.e.

$$SS_E = \sum_{i=1}^{n} (y_i - \hat{y}_i)^2, \tag{4.5}$$

$$SS_T = \sum_{i=1}^{n} (y_i - \bar{y}_i)^2, \tag{4.6}$$

$$SS_T = SS_T - SS_E = \sum_{i=1}^{n} (\hat{y}_i - \bar{y}_i)^2. \tag{4.7}$$

In general, the coefficient of determination, R^2, is used to decide whether a regression model is appropriate. R^2 provides an exact match if it is 1.0 and, if the residual increases, R^2 decreases in the range from 1.0 to 0. As the number of variables increases, the residual increases, so that the determination coefficient increases in value. For this reason, the coefficient of determination adjusted, ${R^2}_{ad}$, is used to obtain a more precise regression model judgment. ${R^2}_{ad}$ takes the form:

$${R^2}_{ad} = 1 - \frac{SS_E/(n-k)}{SS_T/(n-1)}, \tag{4.8}$$

where k is the number of design variables.

Although a higher value of R^2 means a better fit, it is possible that the RS is not the correct representation of the actual data. One way to increase R^2 is to increase the degree of the polynomial, but this has other consequences. Figure 4.1 shows that the error, ϵ, decreases by increasing the order of the polynomial, and hence increases the R^2 value. Using high-order polynomials can result in high noise in the regression. In this case, a backward elimination procedure based on the t statistic can be used to discard terms from the high-order polynomial and improve the prediction accuracy. The t statistic of the fitted coefficient is defined as its value divided by an estimate of the standard error of the coefficient [Raymond & Douglas (2002)].

In backward elimination, we begin with the full regression model obtained from the least square method. The t test is performed on all the regression coefficients to determine their influence on the model. A rule of thumb says that regressor terms with an absolute value of larger than 2.0 are significant at a 95% confidence interval. Thus the regressor terms are removed from the model if the regressor's t is smaller than 2.0 and if $R^2{}_{ad}$ increases after the regressor's removal.

Chapter 5

Summary of Papers

This chapter presents a brief summary of the results reported in the nine papers on which this thesis is based.

Paper I

Large Eddy Simulation of the Flow Around a Simplified High Speed Train Under the Influence of a Cross-Wind

In this work an LES was made to solve the flow around a generic train under the influence of side wind at a 90^o yaw angle. The simplified model of Chiu & Squire (1992) was chosen. The cross section profile of the idealized train model is defined by a mathematical equation. The Reynolds number of the flow is $Re = 3 \times 10^5$, based on the height of the train and the incoming air velocity. One objective of this paper was to compare the CFD results with the available experimental data. The second objective was to explore the flow structures around the train in both the time-averaged and instantaneous flow. The third objective was to calculate the aerodynamic forces and moments of the train and to use their history to find the different frequencies of the flow motion. The accuracy of the CFD results is achieved by performing two LES calculations on two different meshes with different numbers of nodes. The two simulations give similar time-averaged pressure distributions on the surface of the train. Small difference is observed on the bottom side face. In general, the fine mesh simulation gives results that agree well with the experimental data. Different visualization techniques are used to visualize the three-dimensional data set. The vortex sheets that shed from the underside and roof of the train are rolled up to form two large separation bubbles, which dominate the lee side flow. The three-dimensional effect of the nose on the stream-wise, roof and bottom faces is confined to the region very close to the nose, while its effect

on the lee side flow pattern is extended to a region of a length of three times the height of the train from the nose tip in the direction of the train length. Three dominating frequencies are found in the Fourier transform of the time history of the lift and side force coefficients. The instantaneous CFD data are used to find small scale flow structures in the boundary and shear layers around the train.

Paper II

LES Study of the Influence of a Train-Nose Shape on the Flow Structures under Cross Wind Conditions

The objectives of this paper were to investigate the influence of the shape of the train nose on flow structures and aerodynamic coefficients. Two train configurations are used. The cross section and the length of the two train models are identical, while one model has a nose length twice that of the other. The long nose model is identical to that used in paper I. The results reported in Paper I are therefore used here. LES was performed on the flow around the short nose train at the same Reynolds number using two different computational grids: coarse and fine meshes. Comparison of the time-averaged flow structures showed that the the three-dimensional effect of the nose on the stream-wise, roof and bottom faces is independent of the shape of the nose and is confined to a small region very close to the nose. On the other side, the flow pattern on the lee side face of the train depends on the shape of the nose. In the case of the short nose, an axial flow is observed on the lee side face moving towards the nose. The flow patterns on the lee side face of the long nose train show that the flow moves axially from the nose tip towards the body of the train. Thus, the effect of the three-dimensional nose flow on the lee side flow patterns extend axially to about 4.5 the train height from the tip of the nose. Massive flow separation is observed on the roof of short nose train. On the other hand, the flow is almost attached to the roof of the long nose train. The instantaneous data are used to calculate the instantaneous aerodynamic coefficients. The time history of the force coefficients is used to find the dominant frequencies of the flow around the long and short nose trains. The short nose train simulations shows highly unsteady and three-dimensional flow around the nose yielding more flow structures in the wake. In general, the shape of the nose of the train proved to have a great influence on both time-averaged and instantaneous flows.

Paper III

Exploring the Flow Around a Generic High Speed Train under the Influence of Side Winds using LES

Here, the LES is made for the flow around the generic train model, which is the same model used in papers I and II, at two different yaw angles: 90^o and 35^o. The Reynolds numbers based on the freestream velocity and the height of the train are 3×10^5 and 3.7×10^5 for the yaw angles of 90^o and 35^o, respectively. The objective here is to investigate the influence of yaw angles on the flow structures and aerodynamic coefficients. The previous studies showed that the flow is similar to the well-known slender body flow at small yaw angles (less than 10). For large yaw angles, the flow around trains is dominated by three-dimensional vortex shading. For moderate yaw angles, the flow changes from that similar to slender body flow to three-dimensional vortex shedding. The results of this paper show that the two kind of flow regimes exist for the flow around the train at a 35^o yaw angle. A very strong steady vortex is found in the upper circulation region which extends to about five train heights from the nose tip along the length of the train body. Several weak vortices shed from the underbody flow along this distance. At about five times the height of the train from the nose tip in the direction of the body of the train, the strong vortex in the upper circulation region detaches from the surface of the train and is shed to the wake flow. The same flow structure is repeated along the train length. Only the three-dimensional vortex shedding flow regime is found in the flow around the train at a 90^o yaw angle.

Paper IV

Exploring the Flow Around a Simplified ICE2 Train Subjected to a 30^o Side Wind using LES

After exploring the flow around a generic train body, presented in paper III, this paper moves a step forward to investigate the flow around a more realistic train shape: the ICE2 train. The train is simplified because it does not include bogies, intergap, spoiler and track. The train is stationary. The LES is made for the simplified ICE2 train under side wind conditions at a 30^o yaw angle. Experimental data have been collected on a similar model at a Reynolds number of $Re = 1.4 \times 10^6$. The LES Reynolds number is 2×10^5. Despite the seven times lower Re, the LES results are in good agreement with the experiment. Some dis-

crepancies were found, which are related to some differences between the experimental set-up and the computational domain. The two flow regimes that appeared around the generic train in paper III are also found here. The weak vortices that shed from the underbody are attached and detached from the surface of the train in a regular manner, leaving a disturbance in the surface pressure. The most dominant frequency appearing in the power spectra is related to this flow mechanism. The low energetic frequencies that appear in the power spectra are caused by the three-dimensional vortex shedding. The results of this paper are in agreement with previous Detached-Eddy Simulations (DES) that were made for the flow around the model at higher Re (five times more than the LES Re). The LES data provide a time-averaged picture, which is different from what was traditionally believed by experimentalists.

Paper V

DES of the Flow Around a Realistic Bus Model Subjected to a Side Wind with a 30^o *Yaw Angle*

A Detached-Eddy Simulation (DES) was made of the flow around a 1/10 model of a double-deck bus of the type Scania K112 TL. The bus was subjected to a side wind with a 30^o yaw angle. The Reynolds number of the flow, based on the speed of the side wind and a reference length of $\sqrt{0.1}$ [m], was 1.3×10^6. Detailed flow structures and global quantities such as lift, drag, side force, yaw moment and pressure coefficients were computed. The side force and the yaw moment coefficients agree well with the experimental values while some discrepancies were found for the lift force and drag force coefficients. However, the measured values of the aerodynamic coefficients are between the minimum and maximum values of the computed coefficients during the sampling time.

Different visualization techniques have been used to visualize the flow structures around the model in both the time-averaged and instantaneous flows. A comparison between the flow structures in the time-averaged and instantaneous flows shows the following features:

1- The flow separates on the top side face of the bus forming separation bubbles. These bubbles are more stable and steady in the first two-thirds of the bus length while they are more unsteady in the last third of the bus length.

2- The flow in the lee side face of the bus is completely unsteady and dominated by three-dimensional vortices shed from the upper and the

lower edges as well as the front edge of the lee side face of the bus.

3- The flow underneath the bus is dominated by very small structures shed from the geometric details under the bus.

4- The wheel houses inject flows to the lee-side flow. These flows come from the small pipes drilled on the chassis of the bus that connect the two sides of the wheel houses at the front and back axles. They act as the so called flow control where they destroy the formation of the lower part of the recirculation bubble in the lee side flow.

5- Small, unsteady structures are formed in the near wake behind the bus. These structures are shed from the separation bubbles at the edges of the back face. The time-averaged shape of these structures is an upside down arch shaped vortex.

6- All the structures around the bus merge together in the wake behind the bus to form a strong swirling flow downstream of the wind tunnel in the direction of the free stream flow.

The power spectra of the aerodynamic coefficients show that the most dominant frequencies of the flow around the bus are in the range of a Strouhal number between $0.2 < St < 0.4$. A slightly lower dominant frequency is reported for the lift force coefficient. The root mean square value of the side force coefficient is about three times larger than that of the other aerodynamic coefficients.

Paper VI

Transient Simulation of the Aerodynamic Response of a Double-Deck Bus in Gusty Winds

The purpose of the research reported in this paper was to investigate the aerodynamic response of a 1/10 model of a double-deck bus of the type Scania K112 TL in a gusty wind using a Detached-Eddy Simulation (DES). The bus was moving at a 57 m/s and was subjected to three different scenarios of wind gusts: gust in a wind tunnel, gust in a natural wind and gust behind the exit from a tunnel. The proposed scenarios of gusts are in the time domain and take into account the dynamic behavior of natural winds. The Reynolds number of the flow, based on the time-averaged speed of the side wind and a reference length of $\sqrt{0.1}$ [m], was 1.3×10^6. Detailed transient responses of the aerodynamic coefficients and flow structures were investigated. The simulations show that the aerodynamic coefficients fluctuate strongly inside the tunnel. The unsteady flow structures around the bus contribute to these oscillations. The time-averaged values of the aerodynamic coefficients behind the gust were found to be unaffected by the

gust and to approach the values of the aerodynamic coefficients in the case of a steady side wind. For the same Reynolds number and yaw angle, the transient aerodynamic coefficients are different depending on whether the bus is influenced by a gust or a steady side wind. In the case of gust affecting a stationary model in the wind tunnel simulation, the aerodynamic coefficients oscillate strongly during the gust, and the unsteady behavior of the flow appears in a large oscillation in the transient aerodynamic coefficients. The study of the gust at the exit of a tunnel showed that the bus is most resistant to the pitching moment.

Paper VII

On the Aerodynamics of High Speed Trains using Computer Simulations

The objective of this paper was to introduce two approaches aiming to reduce the drag of a train. The first approach is to use the surrogate model as a suitable cheaper methodology for shape optimization. Four different parameters in the front of a two-dimensional train model are optimized. The left force is used as a constraint in the optimization process. The method proved that it is suitable and reliable for shape optimization. The second approach is to use vortex generators to reduce the drag. No greater change in the drag force is observed when the vortex generators are used.

Paper IIX

Aerodynamic Shape Optimization of a Double-Deck Bus Subjected to a 30^o *Side Wind with CFD and Response Surface Models*

In this paper, the CFD based design with a response surface model is proposed to construct the optimum shape of a double-deck bus subjected to a side wind at a 30^o yaw angle. The primary objective was to minimize its aerodynamic coefficients by changing the radius and angle of its front face. A limited number of design points were selected to make CFD simulations based on the Central Composite Design methodology. A second-order polynomial was used to build the response surface out from the CFD simulations. The backward elimination method was used to eliminate some of the regressors from the response surface model to improve its accuracy. The response surfaces constructed were used to obtained the optimal design of the bus to minimize the side force coefficient for a double-deck bus and to obtain Pareto optimal sets. In contrast to what was believed, i.e. that the

streamlined bus could resist side wind (low side force coefficient), the results showed that the optimum design to avoid the unwanted influences of the side wind implies sharp edges on the front of the bus (a cube-like shape). The front angle of the bus was found to have little influence on the aerodynamic coefficients. In general, the CFD-based design with the response surface model shows a promising and cheap alternative to the wind tunnel experiments and the traditional trial-and-error method.

Paper IX

Local Heat Transfer Enhancement Around a Matrix of Wall-Mounted Cubes Using Passive Flow Control: Large Eddy Simulations

The purpose of the research reported in this paper was to investigate the influence of attaching vortex generators (VGs) to a surface of a heated cube on flow structures and heat transfer using large-eddy simulation (LES). The cube was located in the middle of a matrix of similar cubes. Two kinds of vortex generators were investigated. The first was a simple rib extending in the span wise direction (VG1) while the second consisted of several of small cubes (VG2). A mesh topology consisting of C and O-grids was used in the simulations, which considerably reduced the number of cells needed for good spatial resolution. LES results for flow and temperature distributions were obtained for surface mounted cubes with and without a vortex generator. Two computations using different meshes around the cube with VG2 showed mesh independent results. The LES results were found to be in good agreement with the experimental data for the cube without VG, for which experimental data exist.

The paper explains the relation between the flow structures around the cube and the temperature distribution. The stream-wise faces of the cubes were found to have high heat transfer coefficients due to the down-wash flow that efficiently carries the heat from the face. Lower local heat transfer coefficients are reported at places where flow separation occurs, such as at the lee side face of the cube close to the arch shaped vortex.

Attaching vortex generators to the top and lateral faces of the cube resulted in a shorter distance of flow separation at these faces. This led to an increase in the local heat transfer coefficient.

It was found that the VGs altered the boundary layer on the surface of the cube. As a result, vortices were shed from the wake of the VGs at a higher frequency than the dominant vortex shedding in the flow.

Globally, these vortices enhanced the mixing of heat in the boundary layer, which appeared as high mean heat transfer coefficients.

The present investigation showed that the percentage increase in the heat transfer coefficient was considerable with both kinds of vortex generators.

Local high temperature spots were found close to the circulation region behind the rib shaped vortex generator (VG1), but the temperature distribution at the cube with the second vortex generator (VG2) was found to be more evenly distributed. Hence, the problem of local overheating behind VG1 disappeared when VG2 was used.

There was an increase in the mean heat transfer coefficient caused by the attachment of the VG1 and the attachment of VG2 to the surface of the cube of about 13.7% and 16.7%, respectively.

Bibliography

ARIS, R. 1962 *Vectors, Tensors, and Bacis Equations of Fluid Mechanics*, 1st edn. Dover Publications, Inc., iSBN 0-486-66110-5.

BAKER, C. 2003 Some complex applications of the wind loading chain. *Journal of Wind Engineering and Industrial Aerodynamics* **91**, 1791–1811.

BAKER, C., JONES, J., LOPEZ-CALLEJA, F. & MUNDAY, J. 2004 Measurements of the cross wind forces on trains. *Journal of Wind Engineering and Industrial Aerodynamics* **92**, 547–563.

BAKER, C. J. 1991 Ground vehicles in high cross winds, part ii: Unsteady aerodynamic forces. *Journal of Fluids and Structures* **5**, 91–111.

BAKER, C. J. & REYNOLDS, S. 1992 Wind-induced accidents of road vehicles. *Accident Analysis and Prevention* **24** (6), 559–575.

CHELI, F., BELFORTE, P., MELZI, S., SABBIONI, E. & TOMASINI, G. 2006 Numerical-experimental approach for evaluating cross-wind aerodynamic effects on heavy vehicles. *Journal of Vehicle System Dynamics* **44**, 791–804.

CHIU, T. W. 1995 Prediction of the aerodynamic loads on a railway train in a cross-wind at large yaw angles using an integrated two- and three-dimensional source/vortex panel method. *Journal of Wind Engineering and Industrial Aerodynamics* **57**, 19–39.

CHIU, T. W. & SQUIRE, L. C. 1992 An experimental study of the flow over a train in a crosswind at large yaw angles up to 90^o. *Journal of Wind Engineering and Industrial Aerodynamics* **45**, 47–74.

CLARKE, J. & FILIPPONE, A. 2007 Unsteady computational analysis of vehicle passing. *ASME: Journal of Fluids Engineering* **129**, 359–367.

CONSTANTINUESCU, G. & SQUIRES, K. 2003 LES and DES investigations of turbulent flow over a sphere at Re=10,000. *Journal of Flow, Turbulence and Combustion* **70**, 267–298.

COPLEY, J. M. 1987 The three-dimensional flow around railway trains. *Journal of Wind Engineering and Industrial Aerodynamics* **26**, 21–52.

DAVIDSON, P. 2004 *Turbulence*, 2nd edn. Oxford University Press, iSBN 0-19-852949-X.

DEUFRAKU PROJECT 2004 Side wind behaviour of rail vehicles (project no. 19p0056b). [Online], [URL]. http://www.transport-research.info/web/projects/.

DIEDRICHS, B. 2003 On computational fluid dynamics modelling of crosswind effects for high-speed rolling stock. *IMechE* **217** (F), 203–226.

DIEDRICHS, B. 2005 Computational Methods for Crosswind Stability of Railway Trains. Report. Dept. of Mechanical Engineering, Division of Railway Technology, Royal Institute of Technology, Stockholm, SWEDEN.

ESRA, O. & BEDII, O. 2004 Turbulent structure of three-dimensional flow behind a model car: exposed to crosswind. *Journal of Turbulence* **5**, 1–18.

FILIPPONE, A. 2003 Unsteady gust response of road vehicles. *ASME: Journal of Fluids Engineering* **125**, 806–812.

FUJII, T., MAEDA, T., ISHIDA, H., IMAI, T., TANEMOTO, K. & SUZUKI, M. 1999 Wind-induced accidents of train/vehicles and their measures in Japan. Quality report. Railway Technical Research Institude.

HEMIDA, H. & KRAJNOVIĆ, S. 2007 DES of the flow around a realistic bus model subjected to a side wind with a 30^o yaw angle. In 5^{th} *IASME / WSEAS International Conference on FLUID MECHANICS and AERODYNAMICS*. Athens, Greece, 25-27 August.

HEMIDA, H. & KRAJNOVIĆ, S. 2008 LES study of the influence of a train nose shape on the flow structures under cross-wind conditions. *Journal of Fluid Engineering* **130** (9), 091101.

HOPPMANN, U., KOENIG, S., TIELKES, T. & MATSCHKE, G. 2002 A short-term strong wind prediction model for railway application: design and verification. *Journal of Wind Engineering and Industrial Aerodynamics* **90**, 1127–1134.

HOWELL, J. 1986 Aerodynamic response of MAGLEV train models to a crosswind gust. *Journal of Wind Engineering and Industrial Aerodynamics* **22**, 205–213.

HUCHO, W. H. & SOVRAN, G. 1993 Aerodynamics of road vehicles. *Annual Review of Fluid Mechanics* **25**, 483–537.

JEONG, J. & HUSSAIN, F. 1995 On the identification of a vortex. *Journal of Fluid Mechanics* **285**, 69–94.

JUHLIN, M. 2005 A study on crosswind sensitivity of buses. Thesis for Licentiate of Engineering ISSN 1651-7660, 05/32. Dept. of Aeronautical and Vehicle Engineering at The Royal Institude of Technology (KTH), Sweden.

KHIER, W., BREUER, M. & DURST, F. 2000 Flow structure around trains under side wind conditions: a numerical study. *Computers & Fluids* **29**, 179–195.

KOBAYASHI, T. & KITOH, K. 1983 Cross-wind effects and the dynamics of light cars. *International Journal of Vehicle Design,Technological Advances in Vehicle Design Series, SP3, Impact of Aerodynamics on Vehicle Design* pp. 142–157.

KOIKE, M., NAGAYOSHI, T. & HAMAMOTO, N. 2004 Research on aerodynamic drag reduction by vortex generators. Technical review. Mitsubishi Motors.

KRAJNOVIĆ, S. 2002 Large eddy simulations for computing the flow around vehicles. PhD thesis, Dept. of Thermo and Fluid Dynamics, Chalmers University of Technology, Gothenburg.

KRAJNOVIĆ, S. 2007*a* Improvement of aerodynamic properties of high-speed trains by shape optimization and flow control. In 8^{th} *World Congress on Railway Research (WCRR2008)*. Seoul, Korea, May 18-22.

KRAJNOVIĆ, S. 2007*b* Optimization of the aerodynamic properties of high-speed trains with CFD and RSM. In *The Aerodynamics of Heavy Vehicles II: Trucks, Buses and Trains*. Tahoe City, USA, August 26-31.

KRAJNOVIĆ, S. 2007*c* Optimization of vortex generators for drag reduction of a high-speed train. In 7^{th} *International ERCOFTAC Symposium on Engineering Turbulence Modelling and Measurements - ETMM7*. Limassol, Cyprus, 4 - 6 June.

KRAJNOVIĆ, S. & DAVIDSON, L. 2000 Flow around a three-dimensional bluff body. *9th International Symposium on Flow Visualization* .

KRAJNOVIĆ, S. & DAVIDSON, L. 2002 Large-eddy simulation of the flow around a bluff body. *AIAA Journal* **40(5)**, 927–936.

KRAJNOVIĆ, S. & DAVIDSON, L. 2004 Large eddy simulation of the flow around an Ahmed body. In *2004 ASME Heat Transfer/Fluids Engineering Summer Conference*. Charlotte, North Carolina, USA.

KRAJNOVIĆ, S., GEORGII, J. & HEMIDA, H. 2008 DES of the flow around a high-speed train under the influence of wind gusts. 7^{th} International ERCOFTAC Symposium on Engineering Turbulence Modelling and Measurements, ETMM7, 4-6 June, Amathus, Cyprus.

KRAJNOVIĆ, S. & HEMIDA, H. 2007 On the aerodynamics of high-speed trains using computer simulations. In 15^{th} *International Symposium, Towards more Competitive European Rail System*. Ziline, Slovakia, 30 - 31 May.

KRAVCHENKO, G. & MOIN, P. 2000 Numerical studies of flow over a circular cylinder at Re=3900. *Physics of Fluids* **12** (2), 403–417.

MARTINUZZI, R. & TROPEA, C. 1993 The flow around surface-mounted prismatic obstacles placed in a fully developed channel flow. *ASME: Journal of fluid Engineering* **115**, 85–91.

MATSCHKE, G. 2001 Sicherheitsnachweis bei seitenwind. Konzernrichtlinie 401. *Tech. Rep.*. Version 03.2001. Deutsche Bahn AG.

MICHAEL, W., RUBIN, D. & KREMPL, E. 1996 *Introduction to Continuum Mechanics*. Butterworth Heinemann, iSBN 0-7506-2894-4.

MITSUBISHI 2006 Mitsubishi lancer evolution ix. [URL]. http://www.seriouswheels.com/2006/2006-Mitsubishi-Lancer-Evolution-IX-Vortex-Generator-1024x768.htm.

MITTAL, R. & MOIN, P. 1997 Stability of upwind-biased finite difference schemes for large-eddy simulation of turbulent flows. *AIAA Journal* **35** (8), 1415–1417.

NAKAMURA, H., IGARASHI, T. & TSUTSUI, T. 2003 Local heat transfer around a wall-mounted cube at 45 ° to flow in a turbulent boundary layer. *International Journal of Heat and Fluid Flow* **24**, 807–815.

ONLINE 2006 1967 model cessna 182k in flight showing aftermarket vortex generators on the wing leading edge. [URL]. http://www.answers.com/topic/vortex-generator.

PATRICK, G. & CHRISTOPHE, N. 2004 Contribution to the analysis of transient aerodynamic effects acting on vehicles. SAE paper 2004-01-1311.

PERRY, A. E. & CHONG, M. S. 1987 A description of eddying motions and flow patterns using critical-point concepts. *Ann. Rev. Fluid Mech.* **19**, 125–155.

PETZÄLL, J., P.A, T., FALKMER, T., ALBERTSSON, P., & BJÖRNSTING, U. 2008 Aerodynamic design of high-sided coaches to reduce cross-wind sensitivity, based on wind tunnel tests. *International Journal of Crashworthiness* **13**, 158–194.

POPE, S. B. 2001 *Turbulent Flows*, 2nd edn. Campridge University Press, iSBN 0-521-59886-9.

RAGNAR, S. & JONAS, T. 1998 Probabilistic assessment of wind related accidents of road vehicles: a reliability approach. *Journal of Wind Engineering and Industrial Aerodynamics* **74**, 1079–1090.

RAYMOND, H. & DOUGLAS, C. 2002 *Response Surface Methodology*, 2nd edn. WILEY, Inc., ISBN 0-471-41255-4.

RYAN, A. & DOMINY, R. G. 2000 Wake surveys behind a passenger car subjected to a transient cross-wind gust. SAE paper 2000-01-0874.

SHK 2001 Fire in a coach after a traffic accident on highway 70, fjärdhundra, c län, 21st november 1998. (no. ro 2001:04). Swedish Accident Investigation Board (SHK), Stockholm.

SINGH, S. & MITTAL, S. 2005 Flow past a cylinder: shear layer instability and drag crisis. *Int. J. Num. Meth. Fluids* **47**, 75–98.

SUJUDI, D. & HAIMES, R. 1995 Identification of swirling flow in 3-D vector fields. AIAA Paper AIAA 95-1715.

SUZUKI, M., TANEMOTO, K. & MAEDA, T. 2003 Aerodynamic characteristics of train/vehicles under cross winds. *Journal of Wind Engineering and Industrial Aerodynamics* **91**, 209–218.

WILCOX, D. C. 2002 *Turbulence Modeling for CFD*, 2nd edn. DCW Industries, iSBN 1-928729-10-X.

WU, D. 2004 Predictive prospects of unsteady detached-eddy simulations in industrial external aerodynamic flow simulations. Diploma thesis. Matriculation number: 219949. Lehrstuhl fur Strömungslehre und Aerodynamishes Institute, Aachen, Germany.

YAKHOT, A., LIU, H. & NIKITIN, N. 2006 Turbulent flow around a wall-mounted cube: a direct numerical simulation. *International Journal of Heat and Fluid Flow* **27**, 994–1009.

Appendix A

Visualization Techniques

The first step in the analysis of the CFD results is to visualize the flow around the vehicle. This step is very important for understanding the flow structure and highlighting the flow spots that are of special features. Streamlines, path lines, separation and reattachment lines are tools commonly used to visualize the time-averaged surface flow. Different tools (such as local minimum pressure and second invariant of velocity gradient) are used to define the vortex cores in the wake and around the vehicle in both the instantaneous and time-averaged flows. Ensight package for flow visualization is used to visualize the three-dimensional data where most of the flow visualization tools are implemented. The following sections give a short description of the visualization tools used in this work.

A.1 Second Order Tensor Characteristics

The tensor can be defined as a linear transformation of vectors [Michael *et al.* (1996)]. According to this definition, if a vector a_j is transformed to another vector b_i through a linear transformer A_{ij} as in Eq. A.1,

$$A_{ij}a_j = b_i \tag{A.1}$$

then A_{ij} is a tensor.

A.1.1 Rotation Tensor

The rotation tensor is a tensor that transforms vectors in a rigid body rotation manner. That is, the rotation transforms vectors drawn in the rigid body into other vectors. Consequently, there is an infinite number of rotation tensors according to the angle that they rotate the vectors.

A.1.2 Eigenvalues and Eigenvectors of a Tensor

If there is a vector a_j that transforms under a tensor A_{ij} to a vector parallel to itself, i.e.

$$A_{ij}a_j = \lambda a_i, \tag{A.2}$$

then vector a_i is called the eigenvector of the tensor A_{ij} and the constant, λ, is the corresponding eigenvalue. The eigenvector components can be determined in an automatic way if we rearrange Eq. A.2 to be written in the following form

$$(A_{ij} - \lambda\delta_{ij})a_j = 0. \tag{A.3}$$

Equation A.3 is a system of linear homogeneous algebraic equations in a_1, a_2, and a_3. Obviously, regardless of the values of λ, a solution of this system is $a_1 = a_2 = a_3 = 0$. This is known as the trivial solution. This solution simply states the obvious fact that $a_j = 0$ satisfies the equation $A_{ij}a_j = \lambda a_i$, independent of the value of λ. To find the nontrivial eigenvectors for A_{ij}, we note that a homogeneous system of equations admits nontrivial solution only if the determinant of its coefficients vanishes. That is

$$\begin{vmatrix} A_{11} - \lambda & A_{12} & A_{13} \\ A_{21} & A_{22} - \lambda & A_{23} \\ A_{31} & A_{32} & A_{33} - \lambda \end{vmatrix} = 0. \tag{A.4}$$

The above equation is a cubic equation in λ. It is called the characteristic equation of tensor A_{ij}. The roots of this characteristic equation are the eigenvalues of A_{ij}. The eigenvectors can be calculated from equation A.3 using the eigenvalues that have been calculated from Eq. A.4.

If tensor A_{ij} is symmetric, then the three eigenvalues λ_1, λ_2 and λ_3 are real. This gives three real eigenvectors to tensor A_{ij} corresponding to the three real eigenvalues. On the other side, some tensors have eigenvectors in only one direction. For example, for any rotational tensor that affects a rigid body rotation about an axis, only those vectors that are parallel to the axis of rotation will remain parallel to themselves. In general, the antisymmetric real tensors, which have real components like the rotational tensor, have two complex conjugates eigenvalues and one real. The real eigenvalue gives one real eigenvector that is parallel to the axis of rotation.

A.1.3 Principal Invariants of a Tensor

The characteristic equation A.4 can be written as

$$\lambda^3 - P\lambda^2 + Q\lambda - R = 0 \tag{A.5}$$

where

$$\begin{aligned} P &= trA_{ij} \\ Q &= \tfrac{1}{2}(A_{ii}A_{jj} - A_{ij}A_{ji}) = \tfrac{1}{2}[(trA_{ij})^2 - tr({A_{ij}}^2)] \\ R &= det[A_{ij}]. \end{aligned} \tag{A.6}$$

Since by definition the eigenvalues of tensor A_{ij} do not depend on the base vectors, the coefficients of Eq. A.5 will not depend on any particular choice of basis. They are called the principal invariants of tensor A_{ij}.

A.2 Critical Point Theory

It was and is still difficult to visualize the flow field in three-dimensional data sets. This is because turbulent flows are characterized by vortices ranging in size from the integral length scale down to the Kolmogorov scale, and the definition of the vortex is still unclear.

Most of the proposed definitions of vortices are based on the critical point theory. The critical points are points in the flow field where the streamline slope is indeterminate and the velocity is zero relative to an appropriate observer. Asymptotically exact solutions of Navier-Stokes and continuity equation were found close to the critical points, as in the work of Perry & Chong (1987). These solutions give a number of standard flow patterns close to the critical point.

One of the most important parts of the flow visualization is to determine the critical points in both of the instantaneous and the time-averaged flow. In the three-dimensional numerical solution of Navier-Stokes equations, the solution domain is divided to very small cells that may take different shapes. One of these common shapes in computational fluid dynamics is the hexahedral cell, which is commonly used in the structured mesh in the finite volume method. The critical points are found in the cells where the u, v and w components of the velocity vector pass through zero. Taylor series can be used to expand velocity u_i around any arbitrary point, O, inside the cell. This gives

$$u_i = A_i + A_{ij}dx_j + A_{ijk}dx_j dx_k + \ldots\ldots \tag{A.7}$$

Coefficients A_i, A_{ij} etc. are functions of time if the flow is unsteady, and they are symmetric tensors in all indices except the first. If O is located at a critical point, then A_i are equal to zero since the velocity is zero at the critical point relative to an appropriate observer. Moreover, since the cell is very small and infinitesimal, then Eq. A.7 can be truncated at the first-order term. The higher order terms have very little

influence in Eq. A.7 only if the cell size is large. Since we are dealing here with infinitesimal cells, we can use the truncated equation as an exact expression for the velocity field inside the cell. This gives

$$\left.\begin{array}{l} u \approx \frac{\partial u}{\partial x}dx + \frac{\partial u}{\partial y}dy + \frac{\partial u}{\partial z}dz \\ v \approx \frac{\partial v}{\partial x}dx + \frac{\partial v}{\partial y}dy + \frac{\partial v}{\partial z}dz \\ w \approx \frac{\partial w}{\partial x}dx + \frac{\partial w}{\partial y}dy + \frac{\partial w}{\partial z}dz \end{array}\right\}. \tag{A.8}$$

Equation A.8 can be written in the tensor form as

$$u_i = J_{ij}dx_j \tag{A.9}$$

where J_{ij} is the rate of deformation tensor or velocity gradient tensor, $\partial u_i/\partial x_j$ (Jacobian). The velocity gradient tensor, $u_{i,j}$, can be decomposed into a symmetric part and an antisymmetric part as follows:

$$u_{i,j} = \frac{1}{2}[(u_{i,j} + u_{j,i}) + (u_{i,j} - u_{j,i})]. \tag{A.10}$$

Equation A.10 can be written as

$$u_{i,j} = S_{ij} + \Omega_{ij} \tag{A.11}$$

where S_{ij} is the symmetric part representing the strain rate tensor, i.e.

$$S_{ij} = \frac{1}{2}(u_{i,j} + u_{j,i}) \tag{A.12}$$

and Ω_{ij} is the antisymmetric part representing the rotation or the spin tensor

$$\Omega_{ij} = \frac{1}{2}(u_{i,j} - u_{j,i}). \tag{A.13}$$

It has been proven that the relative velocity, v_i, can be related to the relative position, dx_j, by an antisymmetric tensor, Ω_{ij}. Thus $v_i = \Omega_{ij}dx_j$ represents a rigid body rotation with an angular velocity of ω [Aris (1962)]

Thus the antisymmetric part of the velocity gradient tensor corresponds to rigid body rotation, and, if the motion is a rigid one, the symmetric part of the velocity gradient tensor will vanish. For this reason, tensor S_{ij} is called the rate of strain tensor and its vanishing is necessary and sufficient for the motion to be without deformation, that is, rigid. It should be remembered that the rotation tensor has one real and two complex conjugate eigenvalues.

At the critical point, if the rotation tensor dominates over the rate of strain tensor, then the velocity gradient tensor, $\partial u_i/\partial x_j$, is an antisymmetric tensor. This implies that one of the eigenvalues is real and the other two are complex conjugates. Thus, an attracting spiral-saddle pattern is formed. Equation A.9 supports this theory, since the velocity, u_i, rotates around an axis parallel to the real eigenvector, which corresponds to the real eigenvalue. If the real eigenvalue is zero, then the critical point has absolute zero velocity. Otherwise it moves in the direction of the real eigenvector with a velocity equal to the real eigenvalue. The flow pattern around the critical point in that case is called focus. On the other side, if the eigenvalues and eigenvectors of the velocity gradient tensor, $\partial u_i/\partial x_j$, are real, then three planes can be defined by the eigenvectors, and this will be referred as the eigenvector planes. These planes do not need to be mutually orthogonal and, in general, they are the only planes that contain solution trajectories (i.e. some of the streamlines oscillate to these planes close to the critical points). Figure A.1 shows the different kinds of critical points that can appear in the flow.

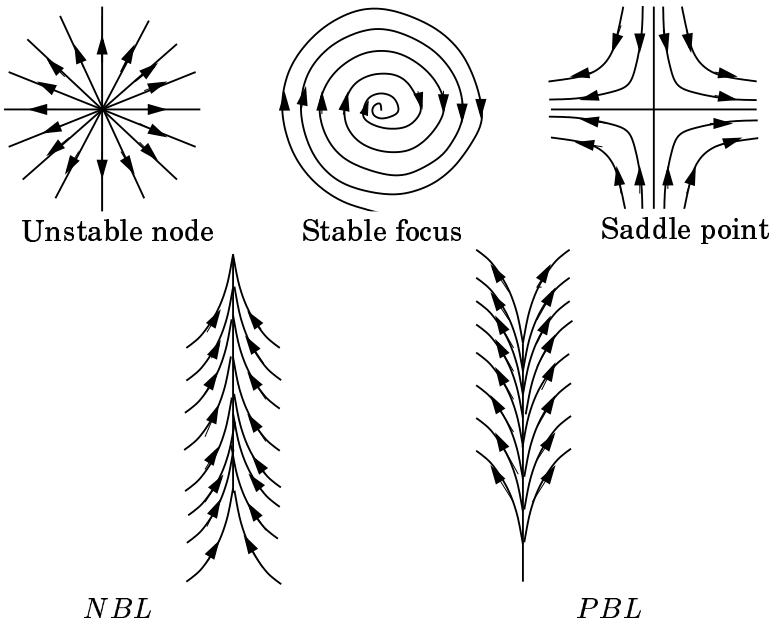

Figure A.1: Schematic representation of an unstable node, stable focus and saddle. NBL and PBL are negative and positive bifurcation lines, respectively.

A.3 Streamlines and Path-lines

Streamlines and path-lines are useful tools for visualizing the flow, especially on the model surface, since the separation and reattachment lines can easily be detected. Vortex can be also detected using streamlines as each pair of separation and reattachment lines has an associated vortex core. Streamlines can, together with velocity vectors projected on the surface, be used to identify critical points. However, there is a problem in terms of of predicting the critical points in the time-averaged three-dimensional data sets far from the surface since the streamlines are not Galilean invariant.

A.4 Vortex Core

Since the turbulence is viewed as a tangle of vortex filaments and most of turbulence physics is well explained using the concept of vortex dynamics, a definition of a vortex could be used for flow visualization. Although the concept of a vortex is very old, we still lake a definition of it. As a consequence, different vortex definitions are proposed in the literature. Jeong & Hussain (1995) summarized the different definitions for vortex core and proposed a new definition based on the following requirements:
(1) The vortex core must have net vorticity.
(2) It should be Galilean invariant.
They found that the intuitive indicators of vortices such as local pressure minimum, closed or spiraling streamlines and path-lines, and isovorticity surface are inadequate and not suitable tools for detecting vortices in an unsteady flow.

A.4.1 Region of Constant Vorticity Magnitude

Vorticity magnitude (ω) has been widely used to educe coherent structure and represent vortex cores [Jeong & Hussain (1995)]. However, this approach is not always satisfactory since $\mid \omega \mid$ does not identify vortex cores in shear flow, especially if the background shear is comparable to the vorticity magnitude within the vortex. Thus, a $\mid \omega \mid$ at a sufficiently low level is necessary but not sufficient to detect a vortex in both free and wall-bounded free shear flows [Jeong & Hussain (1995)].

A.4.2 Region of Complex Eigenvalues of Velocity Gradient Tensor

The critical point theory can be used to identify the center of the swirling flow (i.e. vortex core). According to the theory, the eigenvalues and eigenvectors of the rate of deformation tensor, $\partial u_i/\partial x_j$, evaluated at the critical point define the flow pattern about that point. Specifically, if the eigensystem displays one real and one pair of complex-conjugate eigenvalues, the flow forms a spiral-saddle pattern. The two eigenvectors corresponding to the pair of complex-conjugate eigenvalues define the plane on which the flow swirls, while the eigenvector corresponding to the real eigenvalue points in the direction about which the flow spirals. The eigenvalues, λ, of the velocity gradient tensor, $u_{i,j}$, satisfy the characteristic equation Eq. A.5 where

$$\begin{aligned} P &= u_{i,i} = 0 \\ Q &= \tfrac{1}{2}[(u_{i,i})^2 - u_{i,j}u_{j,i}] \\ R &= det[u_{i,j}] \end{aligned} \tag{A.14}$$

are the three invariants of $u_{i,j}$. The vortex core can be defined as the region of complex λ that will occur when the discriminant, Δ, of Eq. A.5 is positive, i.e.

$$\Delta = (\frac{1}{3}Q)^3 + (\frac{1}{2}R)^2 > 0. \tag{A.15}$$

The above criteria have been used by Sujudi & Haimes (1995) to develop an algorithm to automatically locate the center of the swirling flow in a three-dimensional vector field. The algorithm uses only tetrahedral cells, with all other cell types reduced to two or more tetrahedrals. It evaluates the velocity distribution inside the cell using linear interpolation of four node points of the tetrahedral in the form:

$$u_i = c_i + \frac{\partial u_i}{\partial x_j}\Delta x_j. \tag{A.16}$$

The rate of deformation tensor is simply the coefficient of the linear interpolation velocity vector. The algorithm checks the eigenvalues for each tetrahedral cell in the computational domain. If there is a cell where one real and a pair of complex conjugate eigenvalues for the rate of deformation tensor are found, then a vortex core passes through it.

A.4.3 Region of Positive Second Invariant of Velocity Gradient

The second invariant of the velocity gradient, Q, is defined in Eq. A.14 as

$$Q = \frac{1}{2}\left[(u_{i,i})^2 - u_{i,j}u_{j,i}\right]. \tag{A.17}$$

For incompressible flow, $u_{i,i} = 0$, this gives

$$Q = -\frac{1}{2}u_{i,j}u_{j,i} = \frac{1}{2}\left(\|\Omega\|^2 - \|S\|^2\right) \tag{A.18}$$

where $\|S\| = \left[tr\left(S_{ij}{S_{ij}}^t\right)\right]$, $\|\Omega\| = \left[tr\left(\Omega_{ij}{\Omega_{ij}}^t\right)\right]$ and S_{ij} and Ω_{ij} are the symmetric and antisymmetric components of the velocity gradients as defined in Eq. A.12 and Eq. A.13, respectively. Thus Q represents the local balance between the shear strain rate and vorticity magnitude. The region of positive Q implies that the rotation tensor dominates over the rate of strain tensor, i.e. there is a vortex. Moreover, from Eq. A.15, positive Q implies positive Δ, i.e. the condition of $Q > 0$ is more restrictive than $\Delta > 0$.

A.4.4 Region of Negative λ_2

Jeong & Hussain (1995) proposed a new definition of the vortex core based on the local pressure minimum after discarding the viscous effect that can eliminate the local pressure minimum in a flow with vortical motion and also the effect of the unsteady straining, which can create pressure minimum without involving vortical or swirling motion. Using the above criteria, they defined the vortex as the region of the flow that has two negative eigenvalues for tensor ${S_{ij}}^2 + {\Omega_{ij}}^2$. If λ_1, λ_2 and λ_3 are the eigenvalues and $\lambda_1 \geq \lambda_2 \geq \lambda_3$, the definition is equivalent to the requirement that $\lambda_2 < 0$ within the vortex core.

A.4.5 Region of Minimum Local Pressure

The pressure will have a local minimum in the vortex core in the case in which the centrifugal force is balanced by the pressure force. In that case, the local pressure isosurface can be used to identify the vortex core. Unfortunately, in some cases the centrifugal force can be balanced by the viscous force. This will imply that the method in this case fails to identify the vortex. Thus, the existence of a local pressure minimum is neither a sufficient nor a necessary condition for the presence of a vortex core in general [Jeong & Hussain (1995)].

Appendix B

Realizable $k-\epsilon$ Model

B.0.6 The Standard $k-\epsilon$ Model

The standard k- ϵ model is a semi-empirical model based on model transport equations for the turbulence kinetic energy, k, and its dissipation rate, ϵ. The model transport equation for k is derived from the exact equation, while the model transport equation for ϵ was obtained using physical reasoning and bears little resemblance to its mathematically exact counterpart.

The turbulence kinetic energy, k, and its rate of dissipation, ϵ, are obtained from the following transport equations:

$$\begin{aligned} \frac{\partial}{\partial t}(\rho k) + \frac{\partial}{\partial x_i}(\rho k u_i) = \\ \frac{\partial}{\partial x_j}\left[(\mu + \frac{\mu_t}{\sigma_k})\frac{\partial k}{\partial x_j}\right] + G_k - \rho\epsilon \end{aligned} \tag{B.1}$$

and

$$\begin{aligned} \frac{\partial}{\partial t}(\rho \epsilon) + \frac{\partial}{\partial x_i}(\rho \epsilon u_i) = \\ \frac{\partial}{\partial x_j}\left[(\mu + \frac{\mu_t}{\sigma_\epsilon})\frac{\partial \epsilon}{\partial x_j}\right] + C_{1\epsilon}\frac{\epsilon}{k}G_k - C_{2\epsilon}\rho\frac{\epsilon^2}{k} \end{aligned} \tag{B.2}$$

In these equations, G_k represents the generation of turbulence kinetic energy due to the mean velocity gradients. $C_{1\epsilon}$, $C_{2\epsilon}$, and $C_{3\epsilon}$ are constants. σ_k and σ_ϵ are the turbulent Prandtl numbers for k and ϵ, respectively.

The turbulent (or eddy) viscosity , μ_t, is computed by combining k and ϵ as follows:

$$\mu_t = \rho C_\mu \frac{k^2}{\epsilon} \tag{B.3}$$

where C_μ is a constant.

The model constants $C_{1\epsilon}, C_{2\epsilon}, C_\mu, \sigma_k$, and σ_ϵ have the following values:

$$C_{1\epsilon} = 1.44, \;\; C_{2\epsilon} = 1.92, \;\; C_\mu = 0.09, \;\; \sigma_k = 1.0, \;\; \sigma_\epsilon = 1.3 \tag{B.4}$$

These values have been determined from experiments with air and water for fundamental turbulent shear flows including homogeneous shear flows and decaying isotropic grid turbulence.

B.0.7 The Realizable $k-\epsilon$ Model

This model contains a new transport equation for the turbulent dissipation rate, ϵ . Also, a critical coefficient of the model, C_μ , is expressed as a function of mean flow and turbulence properties, rather than assumed to be constant as in the standard model. The realizable $k-\epsilon$ model is substantially better than the standard K-Epsilon model for many applications.

The term "realizable" means that the model satisfies certain mathematical constraints on the Reynolds stresses, consistent with the physics of turbulent flows.

The modeled transport equations for k and ϵ in the realizable k- ϵ model are

$$\begin{aligned} \frac{\partial}{\partial t}(\rho k) + \frac{\partial}{\partial x_i}(\rho k u_i) = \\ \frac{\partial}{\partial x_j}\left[(\mu + \frac{\mu_t}{\sigma_k})\frac{\partial k}{\partial x_j}\right] + G_k - \rho\epsilon \end{aligned} \tag{B.5}$$

and

$$\begin{aligned} \frac{\partial}{\partial t}(\rho\epsilon) + \frac{\partial}{\partial x_i}(\rho\epsilon u_i) = \frac{\partial}{\partial x_j}\left[(\mu + \frac{\mu_t}{\sigma_\epsilon})\frac{\partial \epsilon}{\partial x_j}\right] + \\ \rho C_1 S_\epsilon - \rho C_2 \frac{\epsilon^2}{k + \sqrt{\nu\epsilon}} \end{aligned} \tag{B.6}$$

where

$$C_1 = \max\left[0.43, \frac{\eta}{\eta+5}\right], \quad \eta = S\frac{k}{\epsilon}, \quad S = \sqrt{2S_{ij}S_{ij}} \tag{B.7}$$

In these equations, G_k represents the generation of turbulence kinetic energy due to the mean velocity gradients. C_2 is constant. σ_k and σ_ϵ are the turbulent Prandtl numbers for k and ϵ, respectively.

The k equation is the same as that in the standard k- ϵ model, except for the model constants. However, the form of the ϵ equation is quite different from that in the standard k- ϵ model.

As in standard k- ϵ model, the eddy viscosity is computed from

$$\mu_t = \rho C_\mu \frac{k^2}{\epsilon} \tag{B.8}$$

The difference between the realizable k- ϵ model and the standard k- ϵ model is that C_μ is no longer constant. It is computed from

$$C_\mu = \frac{1}{A_0 + A_s \frac{kU^*}{\epsilon}} \tag{B.9}$$

where

$$U^* \equiv \sqrt{S_{ij}S_{ij} + \tilde{\Omega}_{ij}\tilde{\Omega}_{ij}} \tag{B.10}$$

and $\tilde{\Omega}_{ij} = \Omega_{ij} - 2\epsilon_{ijk}\omega_k$ $\Omega_{ij} = \overline{\Omega_{ij}} - \epsilon_{ijk}\omega_k$ where $\overline{\Omega_{ij}}$ is the mean rate-of-rotation tensor viewed in a rotating reference frame with the angular velocity ω_k. The model constants A_0 and A_s are given by

$$A_0 = 4.04, \quad A_s = \sqrt{6}\cos\phi \tag{B.11}$$

where

$$\begin{aligned} \phi &= \frac{1}{3}\cos^{-1}(\sqrt{6}W), \quad W = \frac{S_{ij}S_{jk}S_{ki}}{\tilde{S}^3} \\ \tilde{S} &= \sqrt{S_{ij}S_{ij}} \quad S_{ij} = \frac{1}{2}\left(\frac{u_j}{\partial x_i} + \frac{\partial u_i}{\partial x_j}\right) \end{aligned} \tag{B.12}$$

It can be seen that C_μ is a function of the mean strain and rotation rates, the angular velocity of the system rotation, and the turbulence fields (k and ϵ).

The model constants C_2, σ_k, and σ_ϵ have been established to ensure that the model performs well for certain canonical flows. The model constants are

$$C_{1\epsilon} = 1.44, \quad C_2 = 1.9, \quad \sigma_k = 1.0, \quad \sigma_\epsilon = 1.2 \tag{B.13}$$

Appendix C

Spalart-Allmaras Model

The Spalart-Allmaras model is a relatively simple one-equation model that solves a modeled transport equation for the kinematic eddy (turbulent) viscosity. The Spalart-Allmaras model was designed specifically for aerospace applications involving wall-bounded flows and has been shown to give good results for boundary layers subjected to adverse pressure gradients.

The model proposed by Spalart and Allmaras solves a transport equation for a quantity, $\tilde{\nu}$, which is a modified form of the turbulent kinematic viscosity. The transport equation for $\tilde{\nu}$ is

$$\begin{aligned} \frac{\partial}{\partial t}(\rho\tilde{\nu}) + \frac{\partial}{\partial x_i}(\rho\tilde{\nu}u_i) &= G_\nu \\ +\frac{1}{\sigma_{\tilde{\nu}}}\left[\frac{\partial}{\partial x_j}\left\{(\mu+\rho\tilde{\nu})\frac{\partial\tilde{\nu}}{\partial x_j}\right\} + C_{b2}\rho\left(\frac{\partial\tilde{\nu}}{\partial x_j}\right)^2\right] &- Y_\nu \end{aligned} \tag{C.1}$$

where G_ν is the production of turbulent viscosity and Y_ν is the destruction of turbulent viscosity that occurs in the near-wall region due to wall blocking and viscous damping. $\sigma_{\tilde{\nu}}$ and C_{b2} are constants and ν is the molecular kinematic viscosity.

The turbulent viscosity, μ_t, is computed from

$$\mu_t = \rho\tilde{\nu}f_{v1} \tag{C.2}$$

where the viscous damping function, f_{v1}, is given by

$$f_{v1} = \frac{\chi^3}{\chi^3 + C_{v1}^3} \tag{C.3}$$

and

$$\chi \equiv \frac{\tilde{\nu}}{\nu} \tag{C.4}$$

The production term, G_ν, is modeled as

$$G_\nu = C_{b1}\rho\tilde{S}\tilde{\nu} \tag{C.5}$$

where

$$\tilde{S} \equiv S + \frac{\tilde{\nu}}{\kappa^2 d^2} f_{v2} \tag{C.6}$$

and

$$f_{v2} = 1 - \frac{\chi}{1 + \chi f_{v1}}. \tag{C.7}$$

C_{b1} and κ are constants, d is the distance from the wall, and S is a scalar measure of the deformation tensor. S is based on the magnitude of the vorticity as:

$$S \equiv \sqrt{2\Omega_{ij}\Omega_{ij}} \tag{C.8}$$

where Ω_{ij} is the mean rate-of-rotation tensor and is defined by

$$\Omega_{ij} = \frac{1}{2}\left(\frac{\partial u_i}{\partial x_j} - \frac{\partial u_j}{\partial x_i}\right) \tag{C.9}$$

The destruction term is modeled as

$$Y_\nu = C_{w1}\rho f_w \left(\frac{\tilde{\nu}}{d}\right)^2 \tag{C.10}$$

where

$$f_w = g\left[\frac{1 + C_{w3}^6}{g^6 + C_{w3}^6}\right]^{1/6} \tag{C.11}$$

$$\begin{aligned} g &= r + C_{w2}\left(r^6 - r\right) \\ r &\equiv \frac{\tilde{\nu}}{\tilde{S}\kappa^2 d^2} \end{aligned} \tag{C.12}$$

C_{w1}, C_{w2}, and C_{w3} are constants. Note that the modification described above to include the effects of mean strain on S will also affect the value of $\tilde{S}$ used to compute r.

The model constants $C_{b1}, C_{b2}, \sigma_{\tilde{\nu}}, C_{v1}, C_{w1}, C_{w2}, C_{w3}$, and κ have the following default values:

$$C_{b1} = 0.1355,\ \ C_{b2} = 0.622,\ \ \sigma_{\tilde{\nu}} = \frac{2}{3},\ \ C_{v1} = 7.1 \tag{C.13}$$

$$C_{w1} = \frac{C_{b1}}{\kappa^2} + \frac{(1 + C_{b2})}{\sigma_{\tilde{\nu}}},\ \ C_{w2} = 0.3,\ \ C_{w3} = 2.0,\ \ \kappa = 0.4187 \tag{C.14}$$